NASA Contractor Report 180847

LEWIS GRANT
IN - 02
120665
P84

An Experimental Mapping of the Flow Field Behind a Glaze Ice Shape on a NACA 0012 Airfoil

Samuel A. Spring
The Ohio State University
Columbus, Ohio

January 1988

NASA

National Aeronautics and
Space Administration

TABLE OF CONTENTS

ACKNOWLEDGMENTS

LIST OF SYMBOLS

c	airfoil chord length.
C_d	two dimensional drag coefficient.
C_p	pressure coefficient.
E	voltage.
E_{corr}	voltage after temperature correction.
E_1	voltage from front side of split film sensor.
E_2	voltage from back side of split film sensor.
K	ratio of E_1 to E_2.
k	nominal roughness element size.
LWC	liquid water content.
M	Mach number.
q	tunnel dynamic pressure.
Q	net heat transferred.
R_e	Reynolds number.
R_w	operating resistance of hot film/wire.
T	total temperature.
T_{cal}	total temperature during calibration of hot film/wire.
T_e	total temperature during hot film/wire data acquisition.

T_s	operating temperature of hot film/wire.
u	velocity component parallel to free-stream velocity.
u'	velocity perturbation in u.
u_e	boundary layer edge velocity parallel to free stream.
U	total velocity vector.
U_{ind}	velocity indicated from hot film/wire before density corrections.
U_∞	free-stream velocity.
v	velocity component perpendicular to free-stream velocity.
v'	velocity perturbation in v.
VMD	volume median droplet diameter in icing condition.
y	distance above airfoil surface measured perpendicular to free-stream.
y_{sep}	distance of separation streamline from airfoil surface.
y_{stag}	distance of stagnation streamline from airfoil surface.
α	airfoil angle of attack.
δ	boundary layer thickness.
δ^*	displacement thickness.
ρ	density of air.
Θ	momentum thickness or hot film/wire pitch angle (depending on context)

CHAPTER I

INTRODUCTION

Aircraft in-flight icing is a problem in aviation and has been the subject of on-going research since the late 1920's [1]. The National Aeronautics and Space Administration (NASA) is currently funding research to predict the aerodynamic penalties of in flight icing. One of the goals of this research is to develop computer codes capable of accurately predicting the aerodynamic characteristics of an airfoil with a rime or glaze ice accretion. Previous experimental data is not detailed enough to rigorously verify the computer codes. The purpose of the current study was to provide such detailed experimental results to test these computer codes.

Aircraft icing occurs when supercooled water droplets impinge on a structure and freeze. If the free-stream conditions are cold enough for the water to freeze upon impact, typically less than 15° F, the resulting ice shape is labeled as rime (figure 1), and causes only limited aerodynamic penalties [2]. Glaze ice results from warmer temperatures when the water runs some distance before freezing. Glaze ice is characterized by the large ice horns that form as a result of

the water running before freezing. These horns induce large laminar separation bubbles that may extend as far back as 20-30 % chord [3]. The penalties incurred by glaze ice is much worse than those by rime ice and can be very dangerous to the aircraft. Airliners have been known to change from normal flight to an inverted dive due to icing of the horizontal tail [4]. In flight experiments have documented the loss of lift and the increase in drag due to aircraft icing [5].

In the past, correlations of the available experimental data have served to predict performance degradations. Brumby [6] has presented broad guidelines for roughness penalties, designed to help flight crews assess the dangers of an icing condition, but these guidelines are qualitative in nature and are not suitable for accurate calculations. In the early 1960's Gray developed a correlation between two dimensional drag coefficient data and several icing parameters [7], but it is for a narrow range of data, and NASA studies have since proved these expressions to be inaccurate out of this range. Bragg [8] has also developed correlations for the drag penalties due to rime ice, but again they cannot be used for glaze ice or over a wide range of icing conditions. An expression for the drag rise due to glaze ice accretions has been developed by Miller, Korkan, and Shaw [9]. However, this correlation lacks an acceptable degree of accuracy. Helicopter rotor icing has been studied extensively by Flemming, et. al. [10]. They have produced correlations of lift and drag to icing conditions

for helicopters. The data base is again small and the scope of the correlations is narrow.

In addition to these correlations, some work has been done to develop computer codes to calculate the iced airfoil performance. For example, the airfoil analysis code of Eppler [11] can be used to predict the performance of rime ice shapes, but it cannot include the surface roughness effects. Bragg [12] in 1984, attempted to modify existing codes to handle both the rime and glaze ice shaped with roughness, but the effort has since been abandoned. The problem with these computer codes is that they cannot accurately compute the large separation regions that occur behind a glaze ice shape.

Research is currently under way to solve the flow field around an iced airfoil using higher order techniques. These techniques are capable of predicting the separation and reattachment regions associated with glaze ice. The Navier-Stokes equations have been solved numerically for the glaze ice shape using the MacCormack algorithm [13], but detailed experimental results are needed for comparison. Potapczuk has also had success in solving the N-S equations for this problem [14]. Cebeci [15] is currently working on an interactive boundary layer approach to solve the flow field for the glaze ice shape, and his approach shows promise.

As each of these codes produce analytical data, an experimental data base is going to be needed to verify these results. Bragg and Coirier [3,16] have produced some experimental data, and the current

3

study is an extension of their work. Preliminary results of this study have been presented in an earlier paper [17].

The following experiment was an attempt to meet the need for detailed experimental data for the verification of the new computer codes. The data generated was for one specific airfoil and ice shape. Lift and drag data were taken to document the overall aerodynamic characteristics of the configuration, and a split-film probe was used to measure the velocity profiles through the separation bubble. Some velocity profiles were also taken downstream of the reattachment point, in the turbulent boundary layer of the airfoil.

CHAPTER II

EQUIPMENT AND PROCEDURES

The primary instrument used in the mapping of the flow field was a single-split, hot-film sensor. Pressure data were also taken to supplement the hot-film data. This section presents an overview of the procedures and equipment used to calibrate, acquire, and reduce the data presented in Chapter III.

EQUIPMENT

The tests were conducted in the Ohio State University's subsonic wind tunnel located at the Aeronautical and Astronautical Research Laboratory (AARL). This tunnel is an open-return tunnel with a test section measuring approximately three feet by five feet by eight feet long. It has a velocity range of 0-220 feet per second, at Reynolds numbers of up to 1.3 million per foot. Tunnel turbulence is reduced using four turbulence screens and honeycomb in the settling chamber. The wind tunnel is set up so that the airfoil model spans the test section from top to bottom.

The model used in this study was a NACA 0012 airfoil with a 21 inch chord. The model was constructed of mahogany and fiberglass in

such a manner that the leading edge could be separated from the main body of the airfoil at the 15% station. A specific ice shape could then be fit precisely onto the main body. At present, only two shapes exists. A clean leading edge shape, and a leading edge shape that simulates a glaze ice formation.

The glaze ice shape used in this experiment was a simulation of a five minute accretion measured on a 21 inch chord NACA 0012 section tested in the NASA Lewis Icing Research Tunnel. The icing conditions were as follows [2]:

$$VMD = 20 \text{ microns}$$
$$LWC = 2.1 \text{ g/m}^3$$
$$T = 18^{o} \text{ F}$$
$$\alpha = 4^{o}$$
$$U_{\infty} = 130 \text{ mph}$$

The resulting accretion was somewhat rough and jagged (see figure 2). The purpose of the simulated shape was only to reproduce the general flow characteristics of the original ice shape. Since the goal of the experiment was to provide verification of computer codes currently under development, the simulated ice shape had to be easy to build and easy to describe numerically. The simulated shape shown in figure 2 accomplished all of these goals.

To document the effect of roughness on the ice shape, two different sizes of roughness were applied to the ice shape for several runs. The first roughness was a 60 grit sandpaper with a nominal roughness element size, k, of 0.012 inches, with a k/c of 0.00057. The other roughness came from 36 grit paper, where $k/c = 0.0011$. The sandpaper was carefully glued to the airfoil surface with special attention being paid to sealing the paper around the pressure taps. Holes were then punched through the paper to open the taps.

The model and leading edge were internally tapped with a total of approximately 90 pressure taps. The ice shape leading edge had a high concentration of taps on the first 40% of the upper surface to better define the separation bubble. Table 1 lists the location of the taps used in the experiment, which also defines the coordinates of the combined airfoil and glaze ice shape.

All of the pressure data were acquired using differential pressure transducers and Scani-valves. The tunnel static and dynamic pressure were measured on Pace transducers, 0-1.0 psid and 0-0.5 psid respectively, while the total pressure in the wake was measured on a Validyne 0-1.25 psid transducer. Pressures from the airfoil taps were measured on a Druck 0-1.0 psid transducer mounted inside of a Scani-valve system. Two 48 port Scani-valves were used, tied in series to a single transducer. Scani-valve data were taken as the tunnel was running, eliminating the need to use cut-off valves.

In the second part of the data acquisition, hot-film data were taken. The hot-film equipment included a hot-film sensor, an anemometer, a traversing mechanism, and a hot-film calibrator.

The sensor was a TSI model 1288 split-film sensor. The split on this film runs parallel to the support. With this type of sensor, end flow is defined as the flow running parallel to the split or at a pitch angle, Θ, equal to zero degrees. Cross flow is then defined at $\Theta = +/- 90^{\circ}$ (figure 3). Split-film sensors have a drawback in that the output is ambiguous, i.e. for any one sample there exists two possible velocity vectors that could produce that output. The ambiguity is in the angle of the velocity vector. Figure 4 shows two different velocities of equal magnitude, one at an angle Θ, the other at an angle $180^{\circ} - \Theta$. Each velocity produces exactly the same output (ignoring support interference). The split film can resolve the magnitude and sign of u, the velocity component perpendicular to the split, but it cannot resolve the sign of v, the component parallel to the split. Therefore the time average of v is meaningless and only the average of v^2 can be measured. Determining the reversal of the stream-wise flow was of utmost importance to this study. The probe had to be run in the cross-flow configuration, with respect to the free stream, in order to pick up this reversal.

The anemometer is the electronics package that controls the hot film and outputs the velocity dependent voltage signal. For this experiment, the anemometer was a TSI model 158 Intelligent Flow

8

Analyzer (IFA 100), capable of controlling up to 16 channels with independent signal conditioning for each channel. For the current set up, only two channels were used, one for each side of the split-film sensor. Overheat ratios of 1.646 and 1.653 were used for channel 1 and channel 2 respectively, resulting in a sensor temperature of 256° C.

The hot film was stepped away from the airfoil surface using an L.C. Smith model BBR30000 traversing mechanism mounted on the side of the tunnel. The traverse was powered by a d.c. motor, and the position was determined by using a potentiometer. The error in the probe position from the model surface should be no more than +/- 0.003 inches or +/- 0.00014 chord lengths. The probe was positioned chord-wise by mounting the first traverse onto a second traverse. The second traverse was also powered by a d.c. motor, but the probe was positioned at a chord-wise station by eye and was accurate to +/- 0.03 inches. In addition to the initial positioning error, the aerodynamic loads deflected the probe downstream by as much as 0.07 inches. This gave a total error in the location of each velocity profile of +0.03, -0.1 inches. In chord lengths, the total error was +0.0048, -0.0014.

Hot films are often calibrated in a small jet of air just large enough to envelope the actual sensor tip in the stream. However, this process works well only if the sensor is both calibrated and used in an end-flow configuration ($\Theta = 0^\circ$). The problem arises because of the interference of the probe supports on the sensor (see appendix). The effect of the interference is not seen in the calibration unless the

probe supports are in the jet. The problem can be avoided by using a larger jet of air during the calibration. For this, a small, ejector-driven tunnel was constructed to provide accurate calibrations at flow angles from -120 to 120 degrees. The calibrator had a closed cylindrical test section measuring four inches in diameter, and was driven using high pressure air from the AARL's high-pressure storage system. A slot in the cylinder of the test section allowed the hot film to be rotated to any angle between -120 and 120 degrees (figure 5). With the slot in the cylinder, it was necessary to build a sealed plexiglass test cabin around the test section to prevent leakage through the slot during a calibration. This also provided a good system for measuring the pitch angle of the sensor. The hot film was mounted on a 90° elbow allowing the support to exit through a circular window in the side of the test cabin. Rotating the window through an angle, changed the pitch of the probe by the same angle.

Two different analog to digital conversion systems were used, one for the pressure data, and another for the hot-film data. Since all of the pressure data were steady-state, the RTP7471 low-level analog-input system was used for these data. The RTP7471 is a 13 bit conversion system and can sample at rates up to 8 khz. The split film had two separate channels, and it was desirable to sample each channel at exactly the same time to avoid problems with high frequency turbulence. Therefore, it was necessary for the A/D system to have a sample/hold capability. This allowed each channel to be sampled at the same time

and the A/D conversion completed after sampling. The Preston high-speed conversion system had this capability and was used for the hot film data acquisition. The Preston gear is a 15 bit system with a maximum sampling rate of 312.5 khz.

All of the data were acquired and reduced on the Harris 800 super mini-computer. The reduction was carried out on an ADM 3A graphics terminal, and hard copy plots were obtained using the Zeta analog pen plotter.

PROCEDURES

The first step was to calibrate the equipment, namely the pressure transducers and the hot film. The calibration of the pressure transducers was fairly straightforward. Each transducer was connected to a water manometer, so that known pressures could be applied to the transducers, and the output voltages recorded. The calibration involved taking a zero-pressure voltage, and then 15-20 other voltage measurements at different pressures. The zero voltage was then subtracted from the other voltages and a slope calculated from the data. This gave a straight line passing through zero as the calibration curve. At this point in the calibration, the calibration resistors were connected in the bridge of the modulator in place of the transducer, and the corresponding voltages recorded. The calibration curve was then used to determine the pressure represented by each of the resistors. At the start of a group of runs, a new zero was taken

and recorded. The calibration resistors were again connected and the voltages recorded. A new calibration curve was then calculated using these voltages and the known pressures that they represented. In the reduction, the new zero was subtracted from the voltage read during the tunnel run, and the calibration slope applied directly. This eliminated any problems caused by a shift in the zero after the transducer was calibrated.

The hot-film calibration used a similar approach, however the actual procedure was more involved. The objective was to hold the sensor in an air stream of known velocity while recording the voltage output. The data were then fit with a suitable curve. In the current experiment, a split film was used. Therefore the calibration involved not only different air speeds, but also different flow directions. Both of these parameters had to be systematically varied in order to generate a complete calibration curve. For the present experiment, the calibration of the split film involved only three flow angles (-90°, 0°, $+90^{\circ}$) at 13 different speeds ranging from 0 to 300 feet per second. At each condition, the voltages were measured from the front and back sides of the hot film, E_1 and E_2 respectively. After correcting for ambient temperature effects, the velocity dependence was fit with a suitable polynomial, and the angle dependence was fit with a sinusoid of the form

$$\sin \Theta = \frac{E_1{}^2 - E_2{}^2 K^2}{(E_1{}^2 - E_2{}^2 K^2)_{max}} \qquad (1)$$

where K is the ratio of the voltages, E_1 to E_2 at $\Theta = 0^\circ$ and is a function of velocity [18]. The denominator is the value at which the difference between the two voltages is at a maximum, i.e. when $\Theta = +/- 90^\circ$, depending on the sign of the numerator (see the appendix for more information on hot films).

The actual data acquisition was broken down into two sets of experiments. The two acquisition steps were necessary because the wake probe and the hot film used the same traversing mechanism and had to be done separately.

First, the pressure data were taken. This involved using two Scani-valves and a wake probe. The Scani-valves were used to measure the pressure from the airfoil taps, as well as to measure tunnel free-stream conditions. The Scani-valves would step to each port and wait for the data to settle to its new value. The acquisition program would wait up to a user-specified dwell time before moving on to the next port. Cut-off valves were not needed since the data was acquired while the tunnel was running. This did, however, introduce an error since the tunnel velocity could fluctuate during the data acquisition. To minimize this error, tunnel q was measured simultaneously with each port on the Scani-valve. The fluctuation in tunnel q was then accounted for in the data reduction. After the Scani-valves had stepped

through all of the ports, the total pressure deficit in the wake was measured one chord length downstream of the trailing edge, to determine the airfoil drag.

The second step involved repositioning the traversing system so that the hot-film data could be taken. The traverse was positioned above a particular chord-wise station of the airfoil in such a way that the hot film could be withdrawn from the airfoil surface (figure 6). At the beginning of every run, the sensor tip was carefully positioned approximately 0.025 inches off of the airfoil surface. The positioning was done by hand with the aid of a gauge that slipped over the neck of the hot film and set the shoulder of the support a known distance from the airfoil surface (see figure 7). The tunnel was then started and the film stepped, by computer control, away from the airfoil. At each point, the computer took 2000 samples from each channel, and moved on to the next point. Fifty points were taken at each chord-wise station. The tunnel was then shut down, the traverse moved to a new chord-wise station, and the process repeated. In this set up, the velocity components, u and v, were the stream-wise and normal velocity components with respect to the free-stream velocity. At an angle of attack not equal to 0°, u was not parallel to the airfoil chord line and v was not perpendicular to the chord line (figure 8). Likewise, the velocity profiles presented in the results were measured perpendicular to the free-stream velocity and not to the chord line.

14

The first step of the data reduction was to convert the raw data into engineering units. These data came from either a pressure transducer, a hot-film transducer, or a slidewire potentiometer. Further reduction involved using the pressure data to calculate tunnel conditions as well as lift and drag, and using the hot-film data to calculate several boundary layer parameters.

The tunnel conditions were calculated from transducers measuring dynamic pressure and static pressure on the north wall of the test section. The tunnel conditions, such as velocity, Reynolds number and Mach number, were calculated in the usual manner for incompressible flow.

All of the model taps were connected to a transducer through the Scani-valve system. Tunnel q and tunnel static were also measured through the Scani-valves. To improve the accuracy of the data reduction, pressure coefficients were calculated using the q obtained from the Scani-valve transducer, instead of the facility transducer. The pressure data were then integrated to obtain the lift and moment coefficients. The momentum deficit of the airfoil was calculated from the total pressure profile through the wake as measured by the wake probe [19]. The deficit was integrated by operated set limits to determine a drag coefficient. The lift and drag was then used to correct the coefficient data for the tunnel wall effects [20].

The slidewire was only used to determine the position of the hot film with respect to the airfoil surface, and to determine the position

of the total probe in the wake. The voltage returned through the acquisition routine was converted into a position in the same manner as the transducer data.

The hot-film data reduction involved several steps. The procedure will be outlined in this section, but some of the details will be left to the appendix. Each run consisted of 200,000 hot film readings, 50 data points with 2000 samples per data point over two channels. The data was reduced sample by sample using the following procedure.

First a temperature correction had to applied to the voltage output from the anemometer. This correction is based on King's Law (see appendix), and was applied separately to each channel of the split film.

$$E_{corr} = \left[\frac{T_s - T_{cal}}{T_s - T_e} \right]^{0.5} E \qquad (2)$$

After the correct voltage was calculated for each channel, the magnitude of the total velocity was calculated from a polynomial curve fit obtained from the calibration. This curve fit was a function of the square of the sums of the component voltages.

$$U = f(E_1 + E_2)^2 \qquad (3)$$

The ratio k was then calculated from another polynomial curve fit, also a function of the same argument.

The flow angle Θ was measured from the split, with negative angles indicating reversed flow. The relation between flow angle and voltage is [18]:

$$\sin \Theta = \frac{E_1^2 - E_2^2 K^2}{(E_1^2 - E_2^2 K^2)_{max}} \qquad (4)$$

The denominator of this expression was the maximum value for the particular case, i.e. the value at $\Theta = 90^{\circ}$ for positive flow, or $\Theta = -90^{\circ}$ for reversed flow.

With the magnitude and direction of the flow now known, the velocity components were calculated.

$$u = U \sin \Theta \qquad\qquad v^2 = (U^2 - u^2) \qquad (5)$$

Notice that the sign of v cannot be determined. This is because the split-film output from a flow at angle Θ will have the same output from a flow at angle $180^{\circ} - \Theta$.

The reduction was carried out for the 2000 pairs of data samples at each point. The u-velocity components were then averaged to obtain the velocity profiles presented in Chapter III. Only the averaged u component has any meaning and therefore is the only component

17

presented. All of the boundary-layer parameters were calculated using only this component.

The first boundary-layer parameter calculated was the displacement thickness.

$$\delta^* = \int_0^\delta (1 - \frac{u}{U_e}) \, dy \qquad (6)$$

The velocity term in this equation is a vector and must include the direction of the flow. This was integrated in the usual manner, using a trapezoidal scheme and assuming the velocity to be equal to zero at the wall. The edge of the boundary layer was assumed to be at the point of maximum velocity in the profile.

Next, the momentum thickness was calculated using the following expression.

$$\Theta = \int_0^\delta \left| \frac{u}{U} \right|_e (1 - \frac{u}{U_e}) \, dy \qquad (7)$$

In this expression, the first occurrence of the term (u/U_e) is an absolute value while the second occurrence is not. This term is a vector and must include the direction of the flow. The integration was carried out using the same method and assumptions used for the displacement thickness.

The stagnation streamline is the streamline that runs through the zero u-velocity component of each velocity profile. This pont was

calculated in each profile by linearly interpolating between the two points just before and just after the flow reversed directions.

Finally, the dividing, or separation streamline was calculated. This is the line that separates the steady state re-circulating separation bubble from the outer flow. The calculation assumes that the mass of fluid circulating in the bubble was constant. The mass flux was then integrated up from the wall until it became zero.

$$\int_0^{y_{sep}} u \, dy = 0 \tag{8}$$

At y_{sep} there was an equal mass flux in the negative direction as there was in the positive direction. This was the location of the separation streamline.

Figure 9 shows some of the boundary-layer parameters graphically.

CHAPTER III

RESULTS

The data presented in this chapter are from pressure and hot-film data acquired at angles of attack of 0, 2, and 4 degrees. Both the upper and lower-surface bubbles are presented. At four degrees, two types of roughness were added to better simulate the natural texture of ice.

PRESSURE DATA

Reference 3 presents a detailed study of the aerodynamic effects of this ice shape on the NACA 0012 airfoil. The C_p distributions for this model at $\alpha = 0$, 2, 4 degrees are presented in figures 10-12. For comparison, the C_p distribution for the clean airfoil is shown in figure 13 with the ice-shape C_p distribution. The separation bubble due to the ice shape can clearly be seen as the constant-pressure region in the pressure plot. The upper surface reattachment point cannot be clearly distinguished since the pressure recovery is so gradual during the reattachment. However, the lower surface reattaches fairly abruptly and is well defined. Notice that the size of the

upper-surface bubble is growing with angle of attack as would be expected. The lower-surface bubble decreases with angle of attack, but not as fast as expected.

Sandpaper roughness was added at $\alpha = 4^{o}$ to better simulate a rough ice surface. Previous studies have shown that roughness has little affect on glaze ice aerodynamics [21], and the present data support these results. Very little difference was seen between the smooth and rough pressure distributions. Figure 14 shows the lift plotted against the angle of attack where the clean airfoil data have been included for comparison. The lift at positive angles of attack, does not change significantly between the smooth and rough ice shapes. This essentially means the roughness has very little effect on the upper surface bubble where the sharp ice horn induces immediate separation. The lower surface horn is more rounded, and separation shows some dependence on the surface roughness at negative angles of attack. The drag data, shown in figure 15, show similar results. At positive angles of attack there are only small changes in the airfoil drag due to roughness, while a significant drag increase is shown at negative angles of attack.

When hot film data were taken, the probe was supported in the bubble through a streamlined strut. This strut had to be rigid enough to keep probe deflections to a minimum, and small enough not to change the flow characteristics of the bubble. To determine the interference effects of the strut on the bubble, pressure distributions were taken

21

with the strut and probe located at several strut locations and compared to the pressure distribution with no strut or probe in the flow (figure 16). In each case the static pressure through the bubble decreased due to the presence of the strut. The data also indicates that the reattachment point is moving forward due to the presence of the strut and probe. Lesser effects were seen when only the strut was in the flow, without the probe (figure 17). These results only show that there is some interference between the probe and the bubble. The actual effect of the probe on the velocity field through the bubble can only be determined with flow visualization techniques or non—obtrusive measurement techniques. Flow visualization techniques have already been used on this configuration [22], but not with the strut in the flow.

SPLIT FILM RESULTS

A single wind tunnel run produced a velocity profile at one chord—wise station, like the one shown in figure 18. Figures 19—21 show the velocity profiles for several chord—wise stations grouped by angle of attack. The height y is measured above the airfoil surface in inches, and the velocity is non—dimensionalized by the free—stream velocity. The zero—flow condition is represented by the vertical line associated with each individual profile. In the upper—surface data, the length of the bubble is growing with angle of attack, as seen in the pressure data. For the lower surface, the length of the bubble again follows

what was seen from the pressure data the bubble shortens as the angle of attack is increased. The reattachment point was calculated from the series of profiles for a particular angle of attack. Reattachment was assumed to be half-way between the last reversed flow profile and the first completely attached profile. Figure 22 shows the reattachment points as a function of angle of attack, with the appropriate error bars.

The stagnation streamlines are the points of zero stream-wise flow and can be traced through the velocity profiles. The stagnation streamlines are plotted in figure 23, on top of the airfoil and ice shape for reference. This streamline represents the centerline of a representative steady state eddy in the separation bubble, where the flow below this line is reversed, on the average. As expected, this region stretches on the upper surface and shrinks on the lower surface with angle of attack.

The dividing streamlines represent the mean size of the separation bubbles. These are shown in figure 24. The bubbles are quite large, especially at the higher angles of attack. Notice the bubble on the lower surface does not decrease in size with angle of attack as fast as might be expected.

All of the profiles were integrated to obtain the boundary-layer displacement and momentum thicknesses. The displacement thickness, δ^*, is plotted in figures 25-26 as a function of x/c for the upper and lower surfaces. As expected, δ^* increases sharply at the beginning of

the bubble and then decreases as it approaches reattachment. But δ^* continues to decrease well beyond reattachment, as far back as 60 percent chord on the lower surface at 0°. Notice that the maximum δ^* changes with angle of attack, but the chord-wise location is constant. This point corresponds very closely to the point where the ice shape meets the airfoil.

Figures 27-28 show the momentum thickness, Θ, for both surfaces. The momentum thickness also increases as it enters the bubble, reaching a maximum and then dropping to a local minimum. The local minimum occurs within the given error of the reattachment point as determined by the velocity profiles. In all but one of the cases, Θ increases to another local maximum, decreases to a second minimum far down the airfoil, and finally starts rising again. The local momentum thickness can be related to the local drag of the airfoil by the expression derived by Squire and Young [23].

$$c_d = \frac{2}{c}\,\Theta\,\left[\frac{U_e}{U_\infty}\right]^{3.2} \tag{9}$$

By differentiating this expression, the change in drag is given as:

$$\frac{d}{dx}c_d = \frac{2}{c}\left[\frac{d\Theta}{dx}\left[\frac{U_e}{U_\infty}\right]^{3.2} + \Theta\,\frac{d}{dx}\left[\frac{U_e}{U_\infty}\right]^{3.2}\right] \tag{10}$$

24

From the pressure distribution, the edge velocity is decreasing through the region beyond reattachment. Therefore a decreasing Θ indicates that the differential element is contributing thrust to the airfoil. This is impossible in a viscous flow with an adverse pressure gradient. Therefore, the data must be incorrect or mis-interpreted. Possibly the complex unsteady reattachment region extends much further downstream than the time averaged data indicates. Additionally, the expression used to calculate Θ takes into account the stream-wise, steady-state momentum only, which is usually a good assumption. However, the source of the error could be in the momentum carried by the v component, or from the momentum carried by the perturbation terms, u' and v'. Analysis of the rms values for the u component indicates that there are large fluctuations in the u component at, and downstream of the reattachment point. For example, the upper surface reattachment point at $\alpha=2^{\circ}$ had an rms value of 20% of the edge velocity. More data will have to be taken past the reattachment point to better understand this problem.

Split-film data were also taken for the case with surface roughness at $\alpha = 4^{\circ}$. Figure 29 shows the velocity profiles with and without roughness at several chord-wise stations. As with the pressure distributions, no significant difference could be seen between the smooth and rough cases.

CHAPTER IV

SUMMARY AND RECOMMENDATIONS

The flow field including the separation bubble behind a simulated glaze ice shape on a NACA 0012 airfoil has been studied. Split-film data were taken on both surfaces to define the bubble. The bubble was defined by measuring the stream-wise velocity profiles at chord-wise stations located approximately every 2-4 percent. Pressure data were also taken to supplement the hot-film data. This included C_p distributions to obtain lift, as well as wake probe measurements to obtain drag. These data were taken at 0, 2, and 4 degrees at a Reynolds number of 1.5 million. Finally, the measurements were repeated at $\alpha = 4^o$ with the 36 grit sandpaper on the ice shape and again with the 60 grit sandpaper.

From these data, velocity profiles were constructed, and several boundary-layer parameters were calculated, namely the displacement thickness, momentum thickness, stagnation streamline, and separation streamline.

Both the pressure distributions and the velocity profiles indicated large separation bubbles as a result of the glaze ice horns.

The lower surface horn was smaller than the upper horn yet still produced a large bubble even at positive angles of attack. At the angles of attack studied, the bubble reattached at some point past the ice shape. As α was increased, the upper surface reattachment point moved toward the trailing edge, and the bubble grew in size. Likewise on the lower surface, the reattachment point moved forward and the bubble decreased in size.

The roughness had little effect on either the pressure results or the hot-film data. Lift and drag measurements indicated the lower surface being affected more than the upper surface by roughness. At negative angles of attack, the maximum lift was decreased and the drag was increased due to the increased separation.

The momentum thickness showed expected trends by increasing at the beginning of the bubble and decreasing towards reattachment, but there is definitely a problem after this point. The edge velocities decreasing with θ implies a negative contribution to drag, which makes no physical sense in this flow. The displacement thickness also started out as expected, increasing through the bubble and decreasing as the bubble reattached. Again the results became confusing at this point. The displacement thickness continued to decrease even though the edge velocities were also decreasing. The results for δ^* and θ should be used with caution until more data can be taken to clarify the problem.

RECOMMENDATIONS

More detailed measurements are needed to better define the separation bubble due to glaze ice. Both the u and v components of velocity need to be measured and considered in the calculations to fully understand the flow field. A laser-doppler system would measure both velocity components while at the same time eliminating the interference problems seen with the hot-films.

A more complete data set is also necessary. The bubble needs to be better defined with more velocity profiles, and the region beyond reattachment needs to be investigated.

This study has only dealt with the time averaged characteristics of the flow field. The unsteady characteristics also warrant investigation. This includes the small scale turbulence and the large scale fluctuations of the bubble and reattachment regions.

TABLE 1
Tap Locations, NACA 0012 with Glaze Ice

Upper Surface		Lower Surface	
X	Y	X	Y
-0.02660	0.01690	-0.01750	-0.00700
-0.02450	0.02870	-0.01070	-0.01840
-0.02220	0.00390	-0.00360	-0.02840
-0.02080	0.03060	0.00000	0.00000
-0.01000	0.02880	0.00590	-0.03930
-0.00010	0.02680	0.02580	-0.05330
0.00000	0.00000	0.03970	-0.05030
0.01000	0.02500	0.04950	-0.04730
0.02210	0.02670	0.06950	-0.04210
0.03110	0.03000	0.07930	-0.04360
0.04070	0.03330	0.08960	-0.04730
0.04910	0.03610	0.10940	-0.04870
0.05950	0.03900	0.11930	-0.05000
0.06940	0.04140	0.14000	-0.05200
0.07940	0.04350	0.20000	-0.05738
0.08910	0.04550	0.24000	-0.05913
0.10970	0.04870	0.28000	-0.05993
0.11970	0.05000	0.32000	-0.05993
0.12969	0.05140	0.36000	-0.05926
0.14000	0.05240	0.40000	-0.05803
0.16000	0.05442	0.44000	-0.05631
0.17000	0.05500	0.50000	-0.05294
0.18000	0.05607	0.56000	-0.04878
0.19000	0.05676	0.60000	-0.04563
0.20000	0.05738	0.70000	-0.03664
0.22000	0.05839	0.75000	-0.03160
0.24000	0.05913	0.85000	-0.02053
0.25000	0.05941	0.90000	-0.01448
0.26000	0.05864	0.95000	-0.00807
0.28000	0.05993	0.97500	-0.00471
0.30000	0.06002	1.00000	0.00000
0.32000	0.05993		
0.34000	0.05967		
0.36000	0.05926		
0.40000	0.05800		
0.42000	0.05700		
0.47000	0.05473		

Table 1 continued

Upper Surface		Lower Surface	
X	Y	X	Y
0.50000	0.05294		
0.53000	0.05095		
0.56000	0.04878		
0.60000	0.04563		
0.70000	0.03664		
0.75000	0.03160		
0.80000	0.02623		
0.85000	0.02053		
0.90000	0.01448		
0.95000	0.00807		
0.97500	0.00471		

Rime Ice
T = -15° F
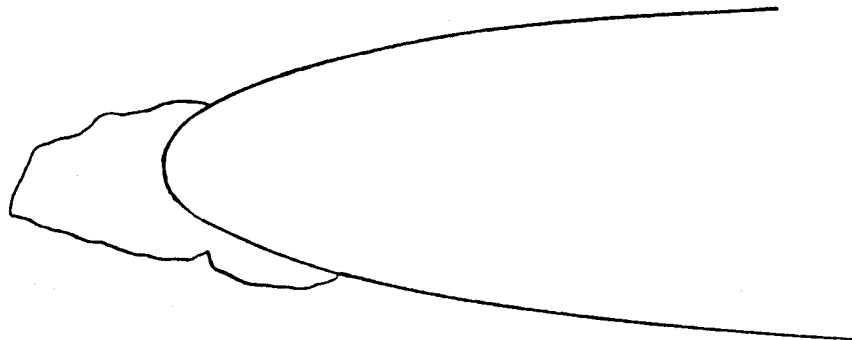
Glaze Ice
T = 18° F
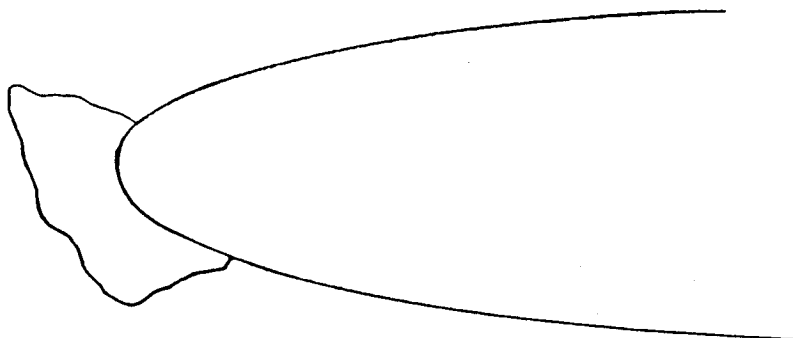
Figure 1.   Example of a rime and glaze ice shape on an
airfoil. Reference 2

31

NACA 0012 Icing Conditions

VMD = 20 μm   LWC = 2.1 g/m^3

T = 18° F U_∞ = 130 mph

α = 4°

5 minute
ice

—————— measured shape
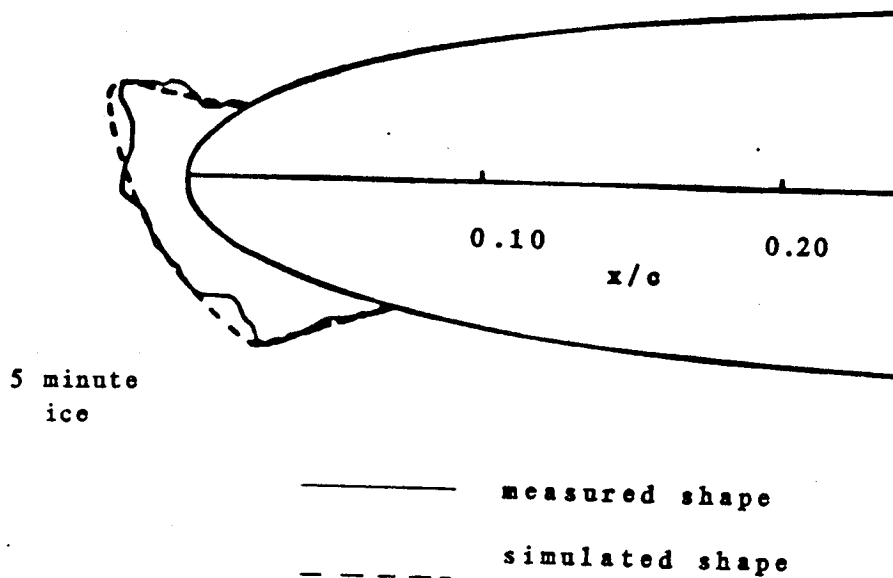
— — — — — simulated shape

Figure 2. Comparison of the measured and simulated ice shape

32
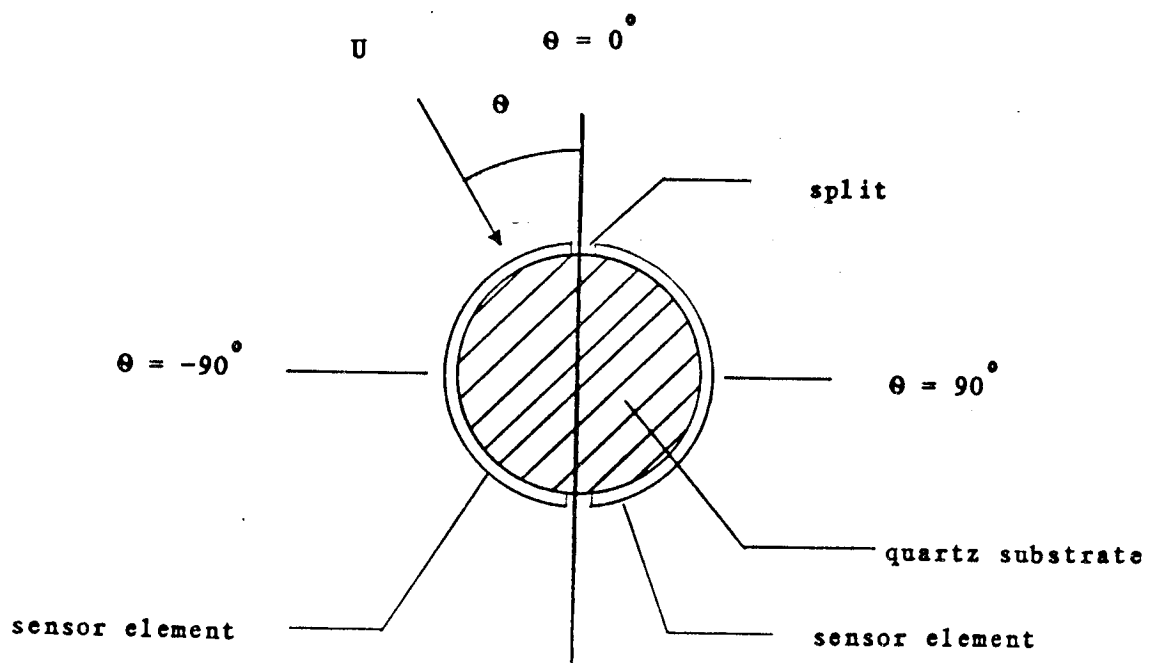
Figure 3. Cross section of split-film sensor element

33
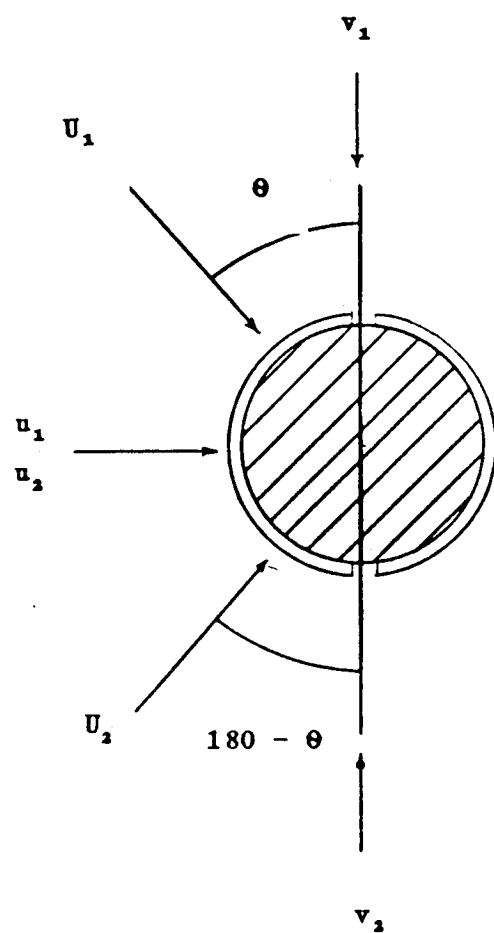
Figure 4. Split film showing identical output from two
           different velocity vectors

34

wake probe traverse
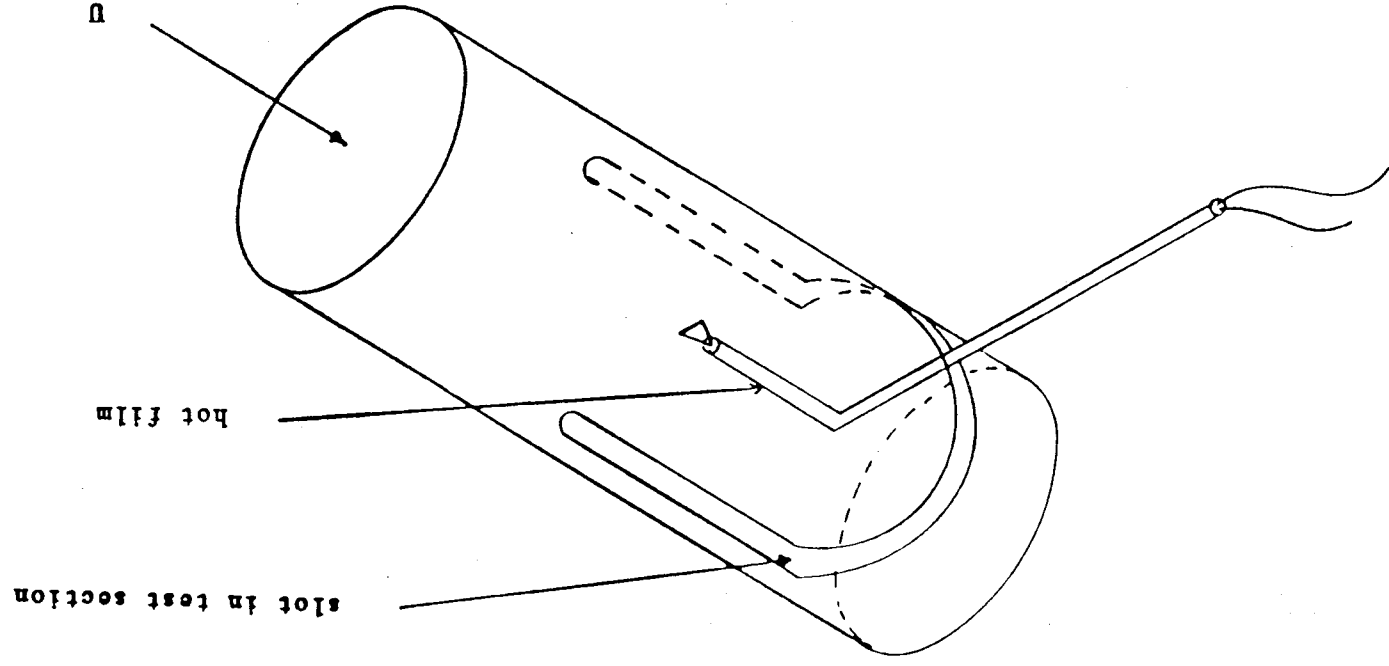
hot-film traverse
with strut in flow

Figure 6. Top view of 3x5 test section showing position of
          traverse mechanism

gauge

0.025 inches

gauge on hot film
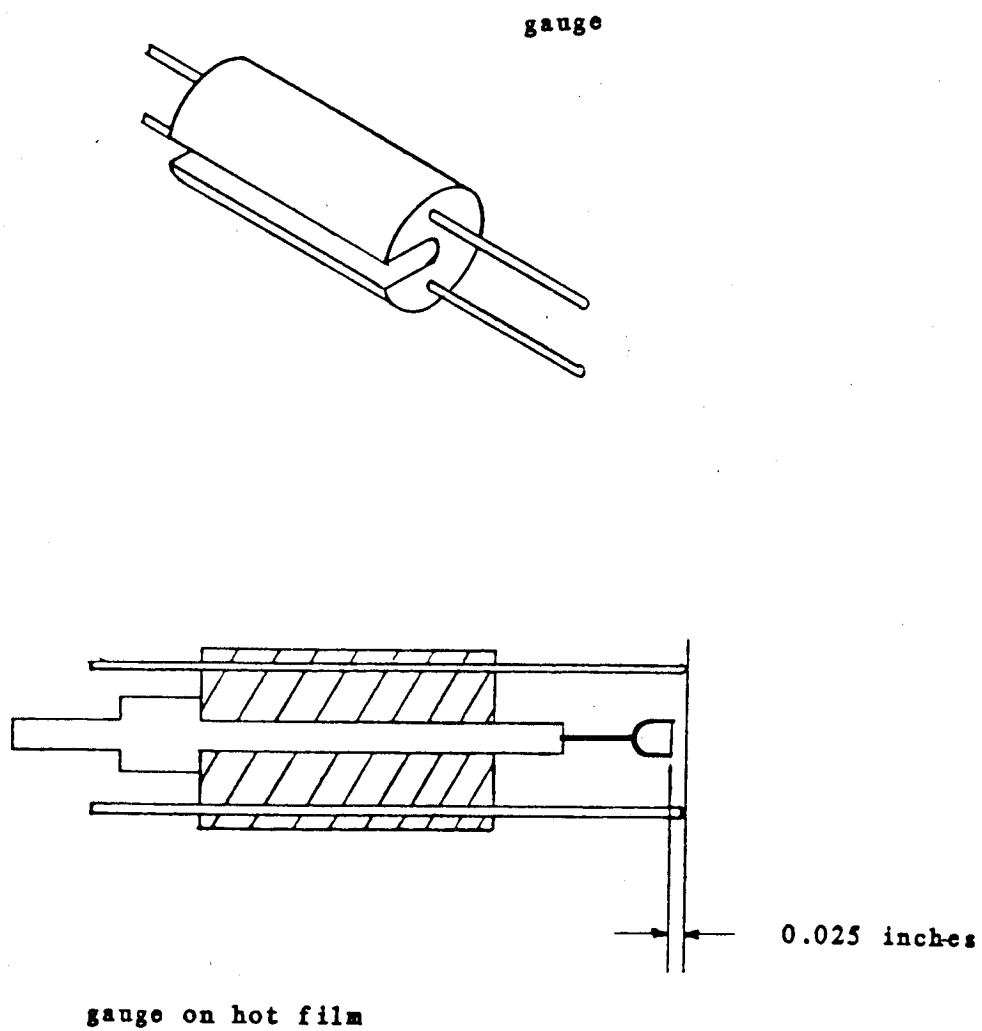
Figure 7. Gauge used for hot-film positioning

probe not to scale

u

v

U_∞

α
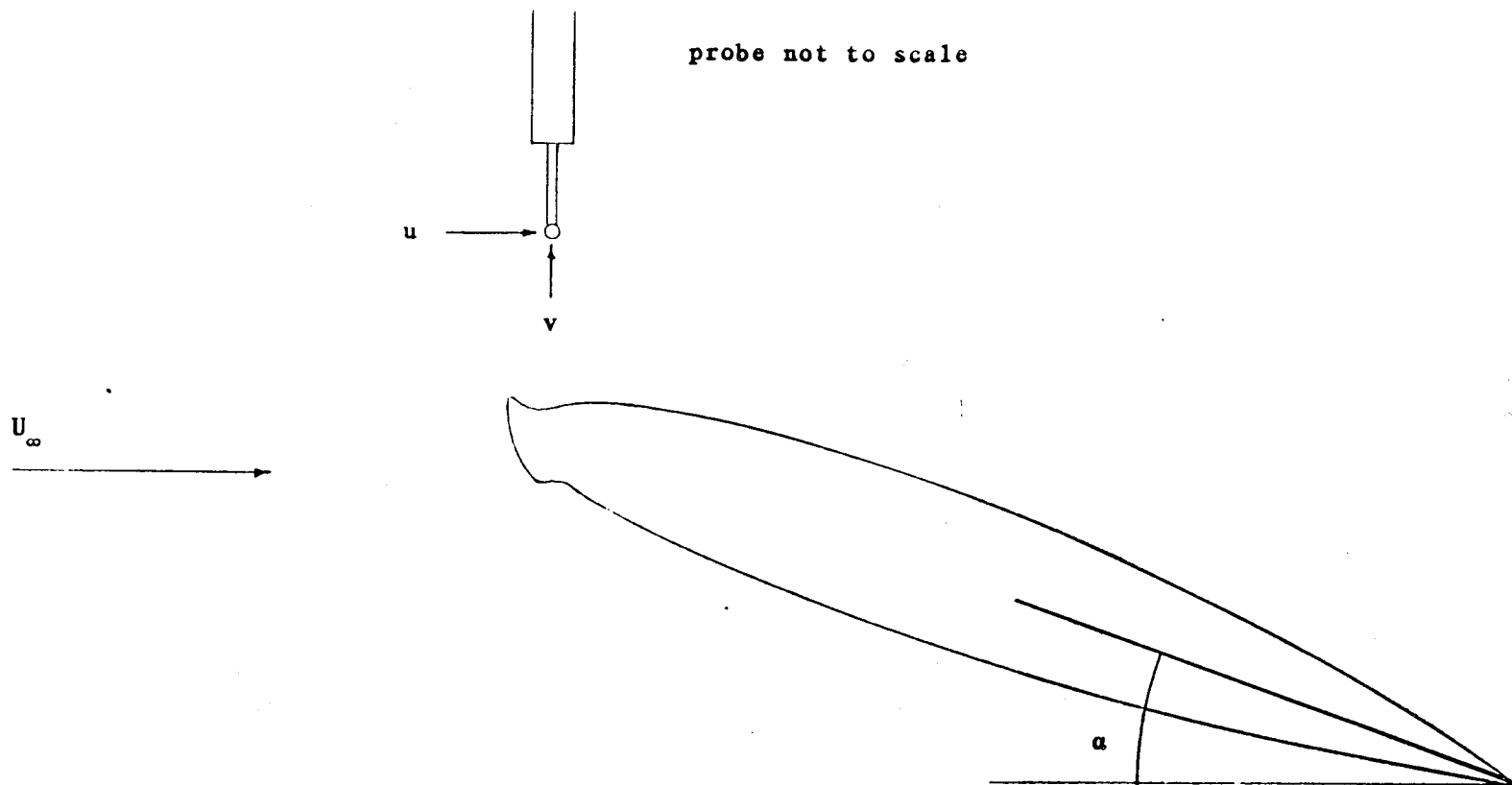
Figure 8.   Probe position relative to airfoil at angle of
             attack
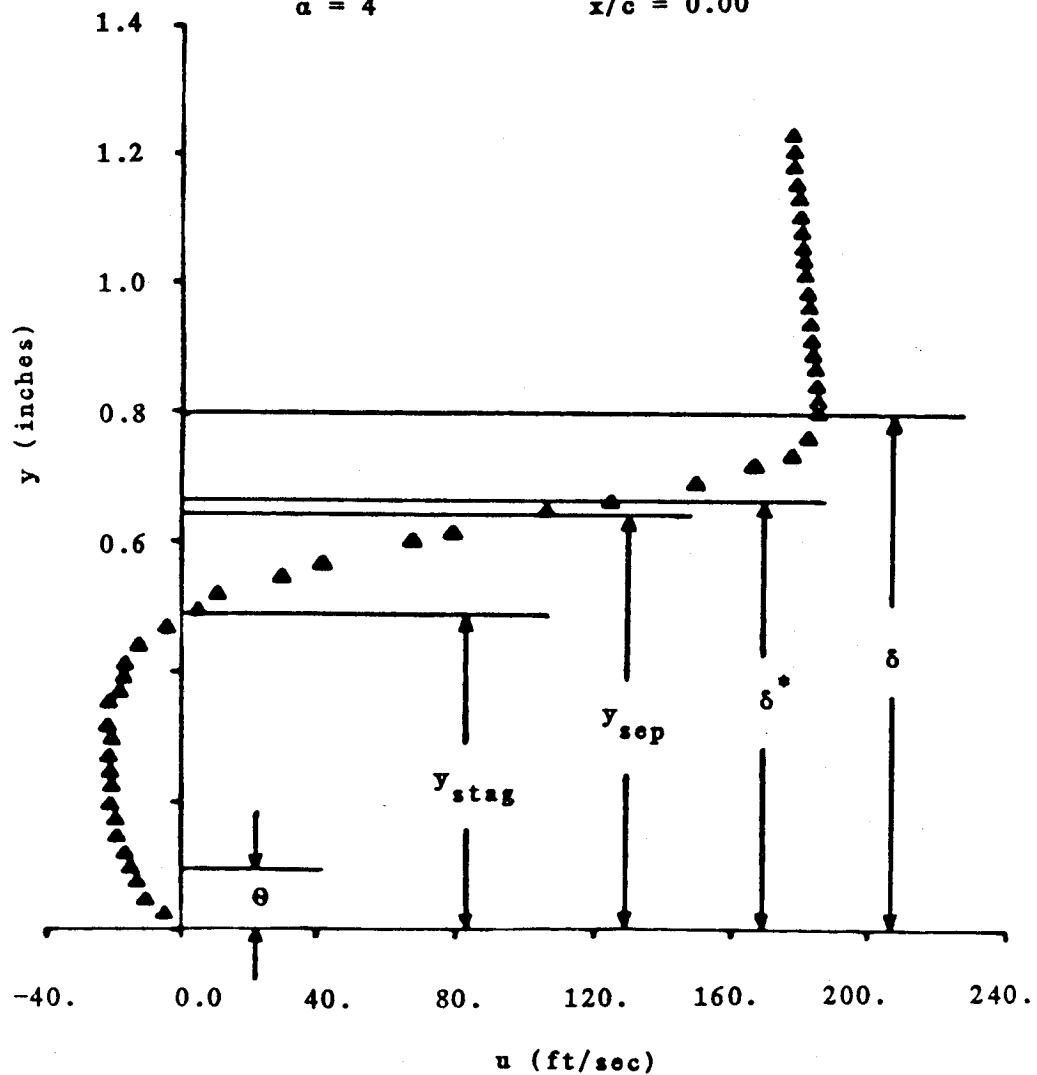
Figure 9. Measured velocity profile in the upper-surface bubble showing boundary layer parameters

NACA 0012 with glaze ice

$Re = 1.5 \times 10^{6}$ $M = 0.12$

$\alpha = 0^{\circ}$
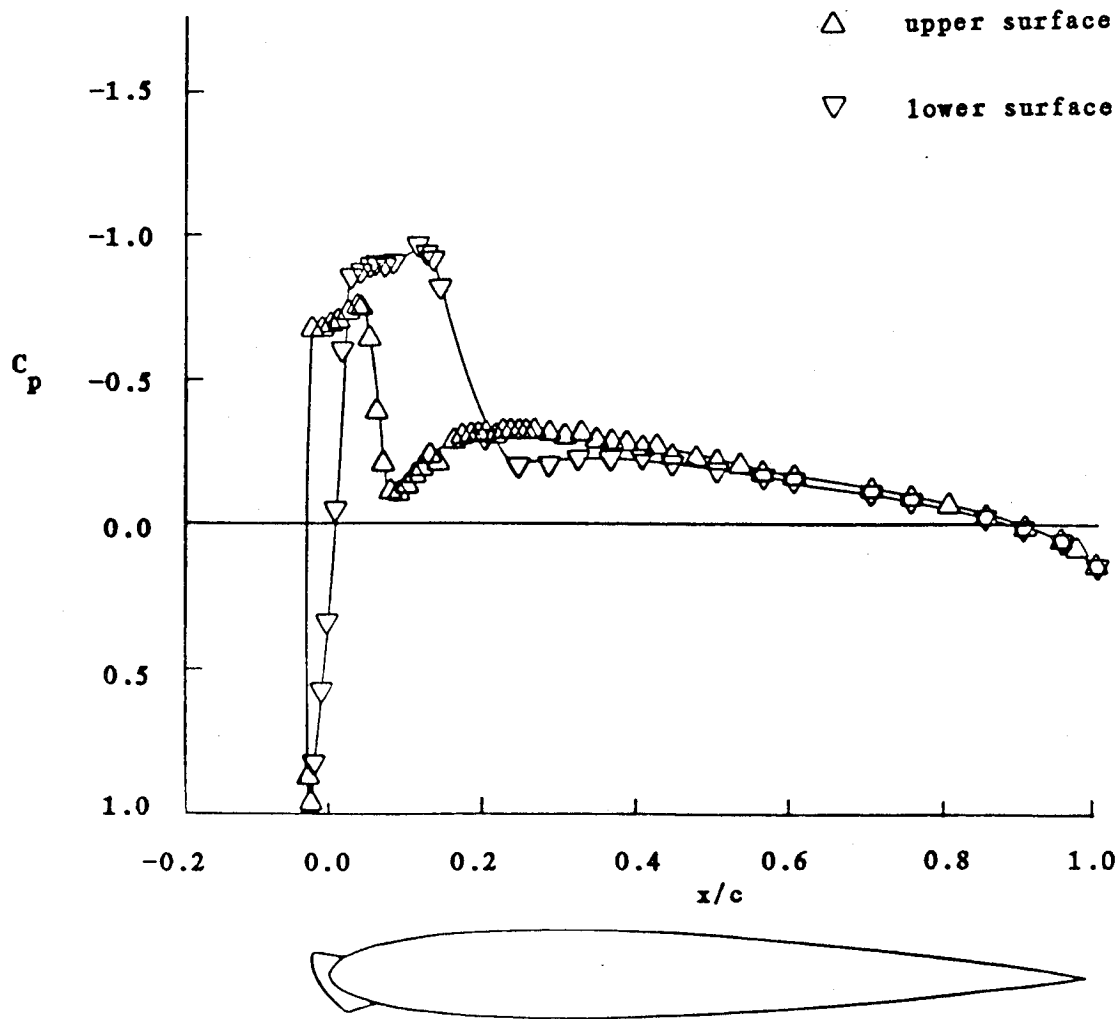
Figure 10. Pressure distribution at $\alpha = 0^{\circ}$

NACA 0012 with glaze ice

$Re = 1.5 \times 10^{6}$ $M = 0.12$

$\alpha = 2^{\circ}$
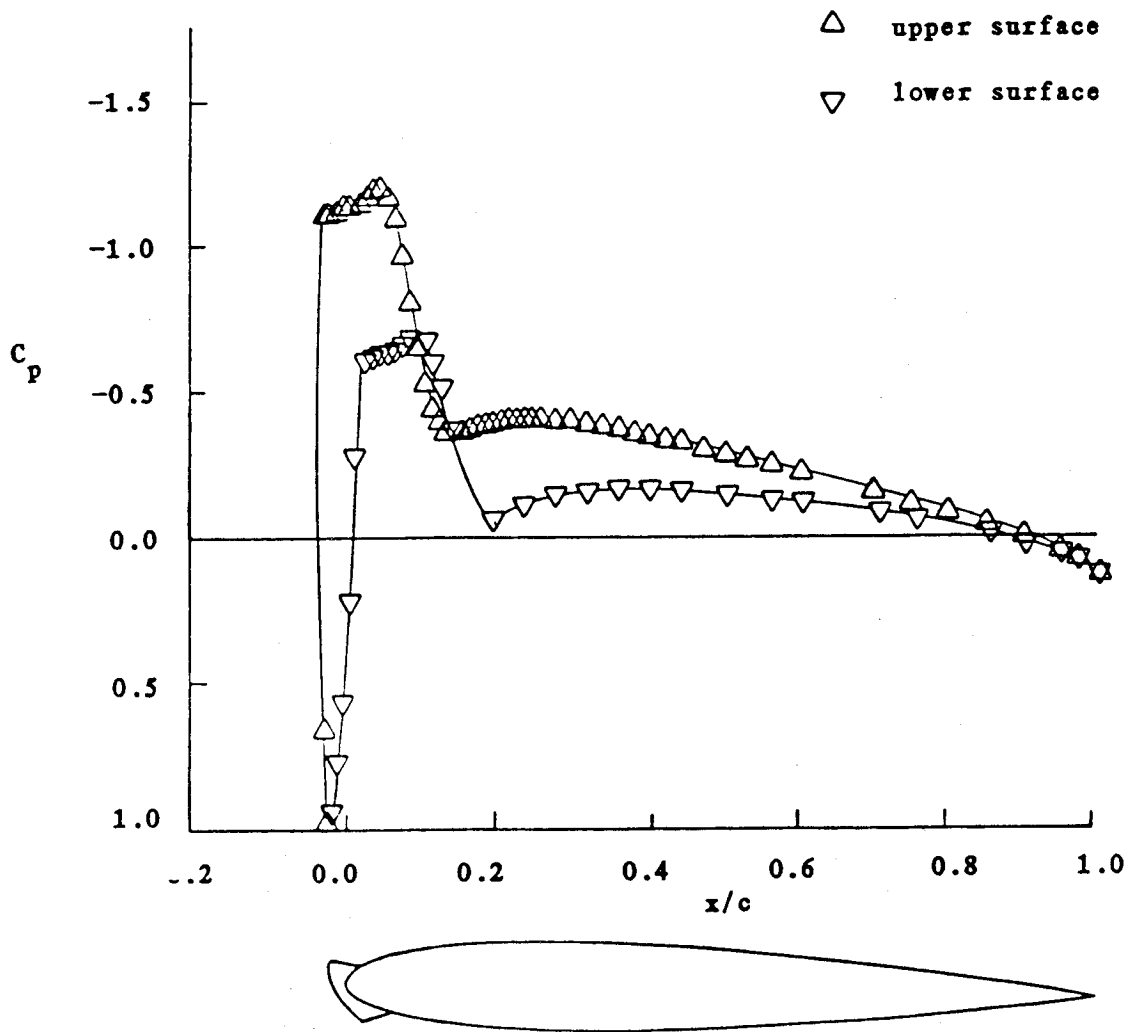
Figure 11. Pressure distribution at $\alpha = 2^{\circ}$

41
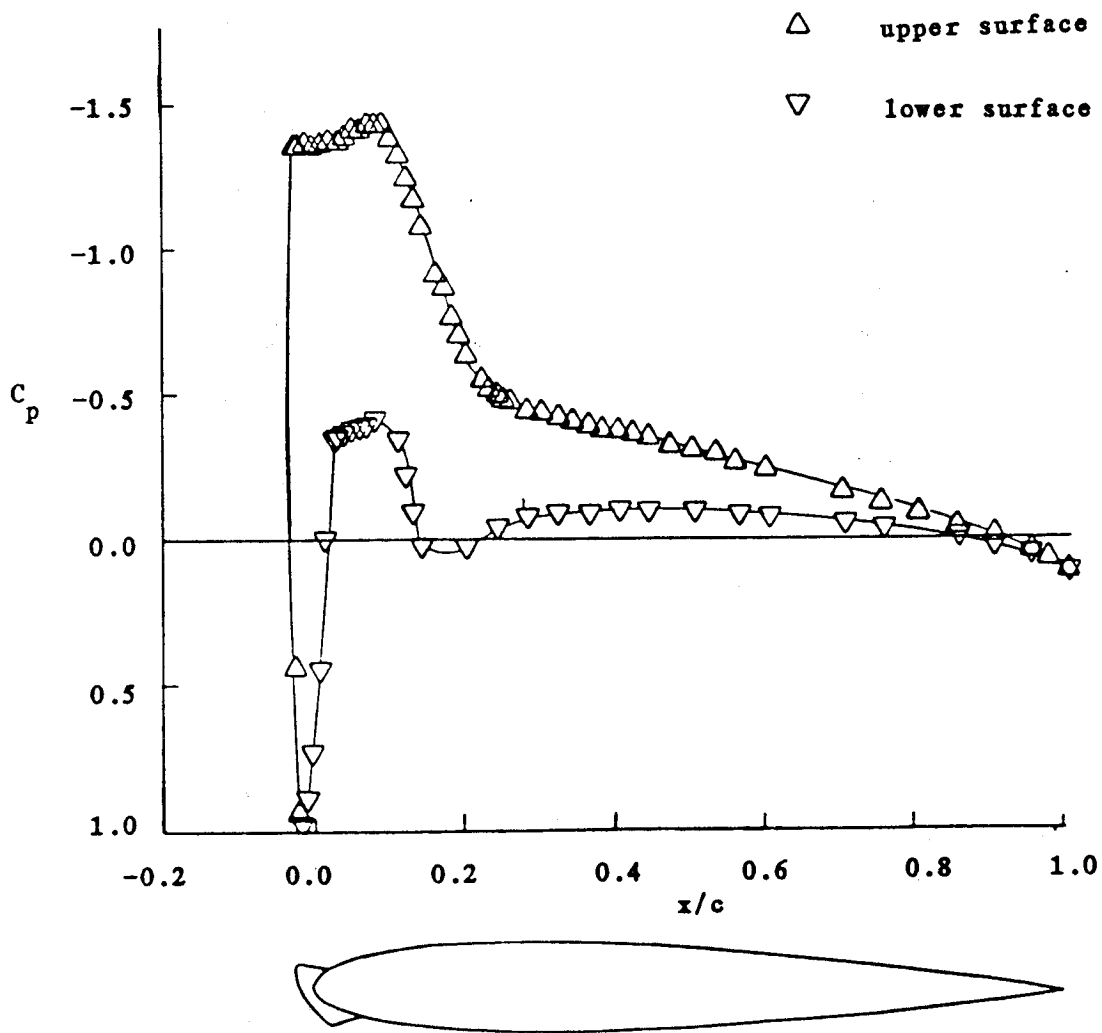
Figure 12. Pressure distribution at $\alpha = 4^{\circ}$

NACA 0012 with and without
Glaze Ice

$Re = 1.5 \times 10^{6}$ $M = 0.12$

$\alpha = 6^{\circ}$

O   clean

□   smooth ice

△   rough ice, $k/c = 0.0011$

C_p
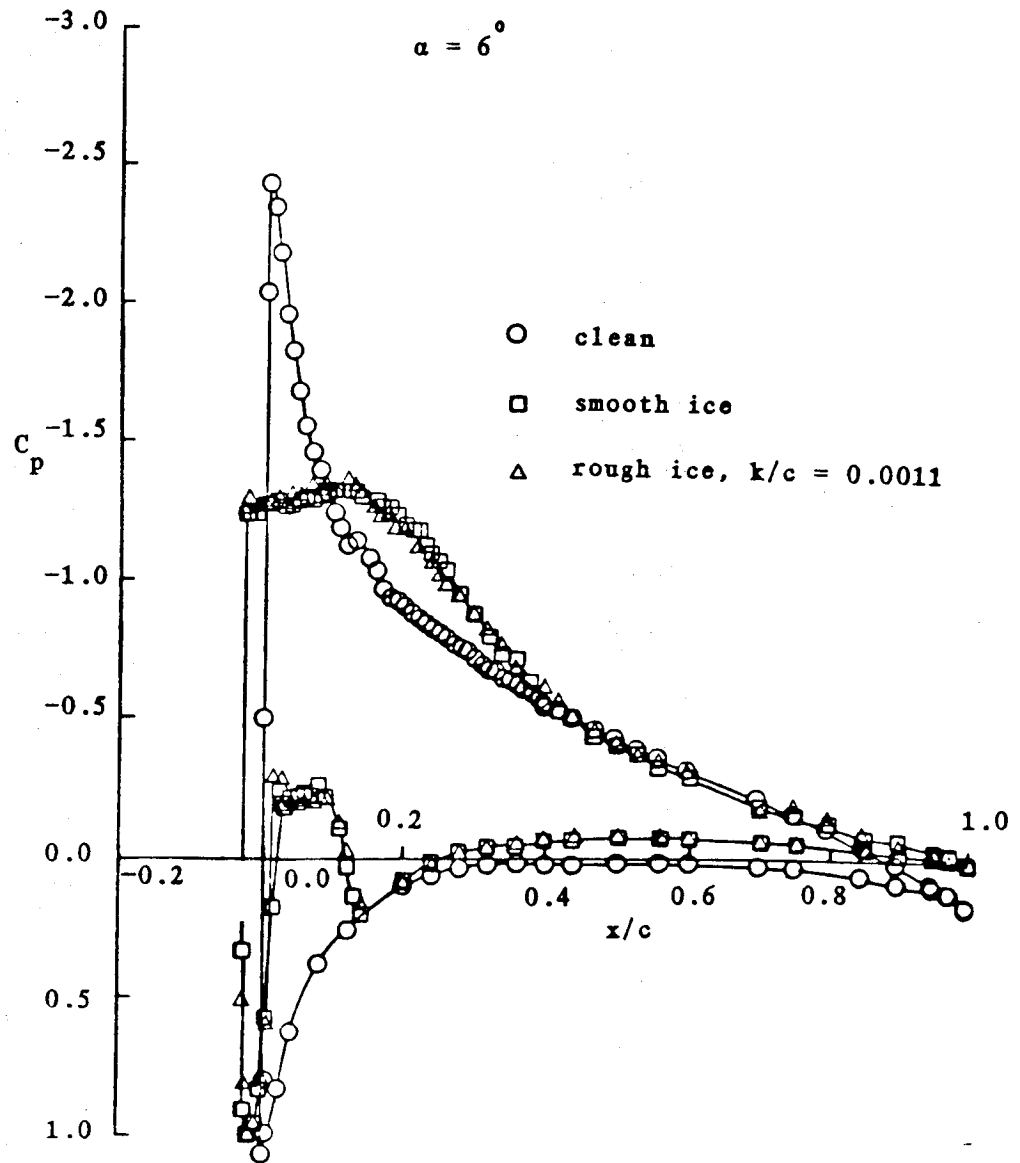
Figure 13.   Pressure distribution for clean airfoil and
iced airfoil

NACA 0012 with glaze ice

$Re = 1.5 \times 10^6$ $M = 0.12$

O clean   △ ice with roughness, k/c = 0.00057

□ smooth ice   ▽ ice with roughness, k/c = 0.0011

C_1

1.50
1.25
1.00
0.75
0.50
0.25
0.00

0   5   10   15

α (deg)

44

C_1

-1.50
-1.25
-1.00
-0.75
-0.50
-0.25
-0.00

0   -5   -10   -15

α (deg)
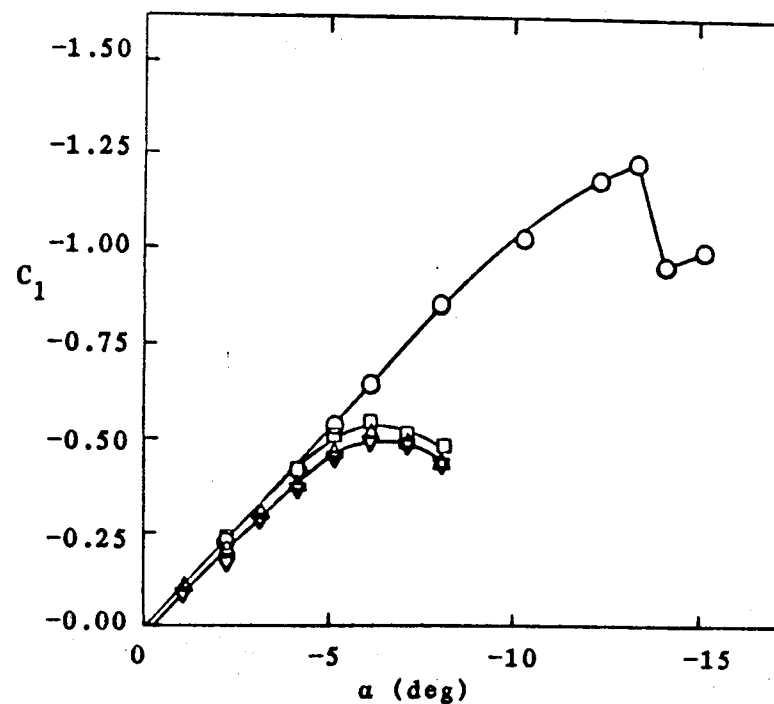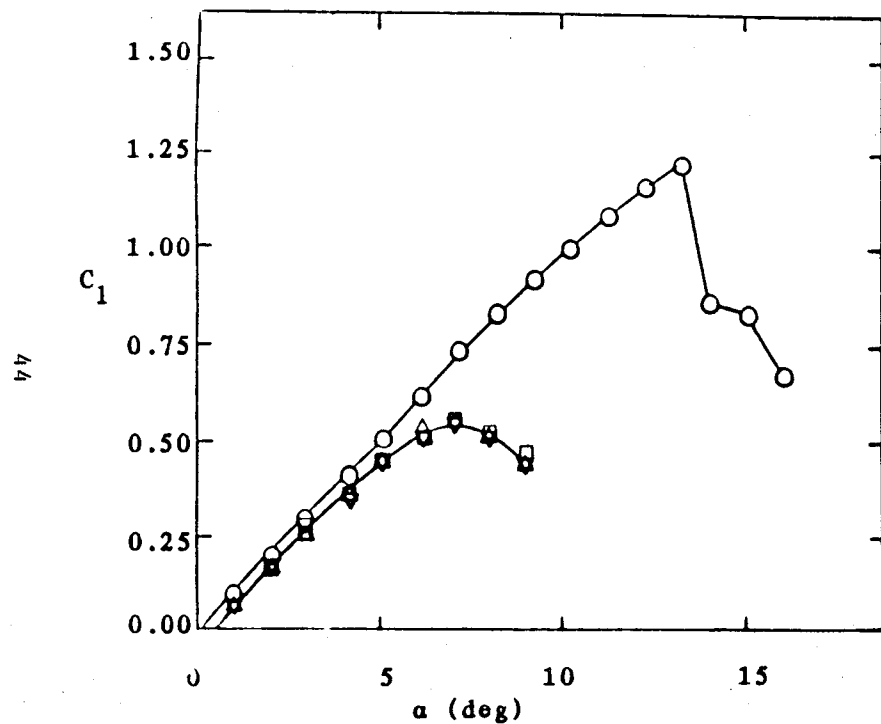
Figure 14. Lift curves of NACA 0012 airfoil including smooth
and rough ice
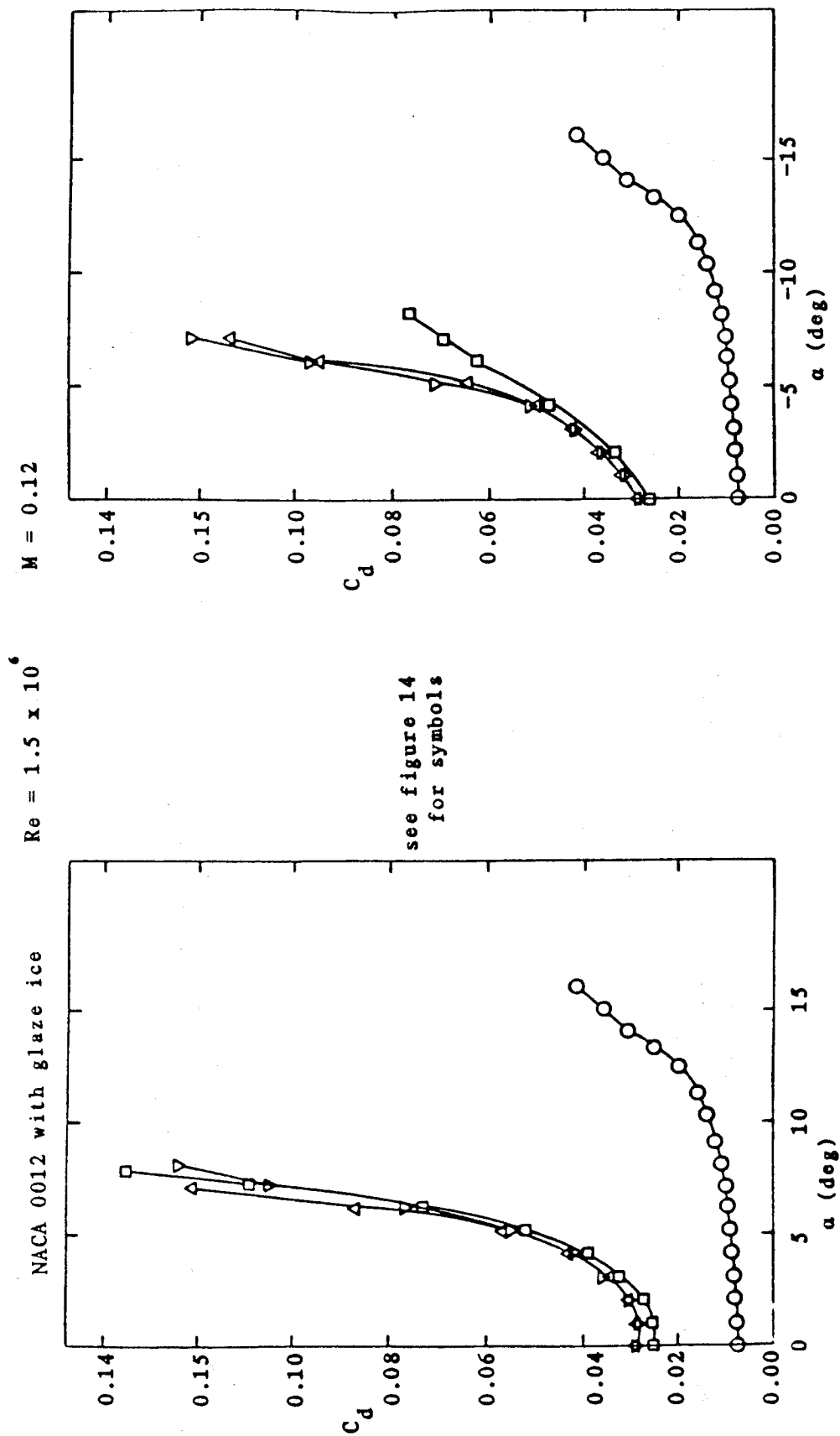
Figure 15. Drag curves of NACA 0012 airfoil including smooth and rough ice

45

NACA 0012 with glaze ice

Re = 1.5 x 10^6 M = 0.12
α = 4°
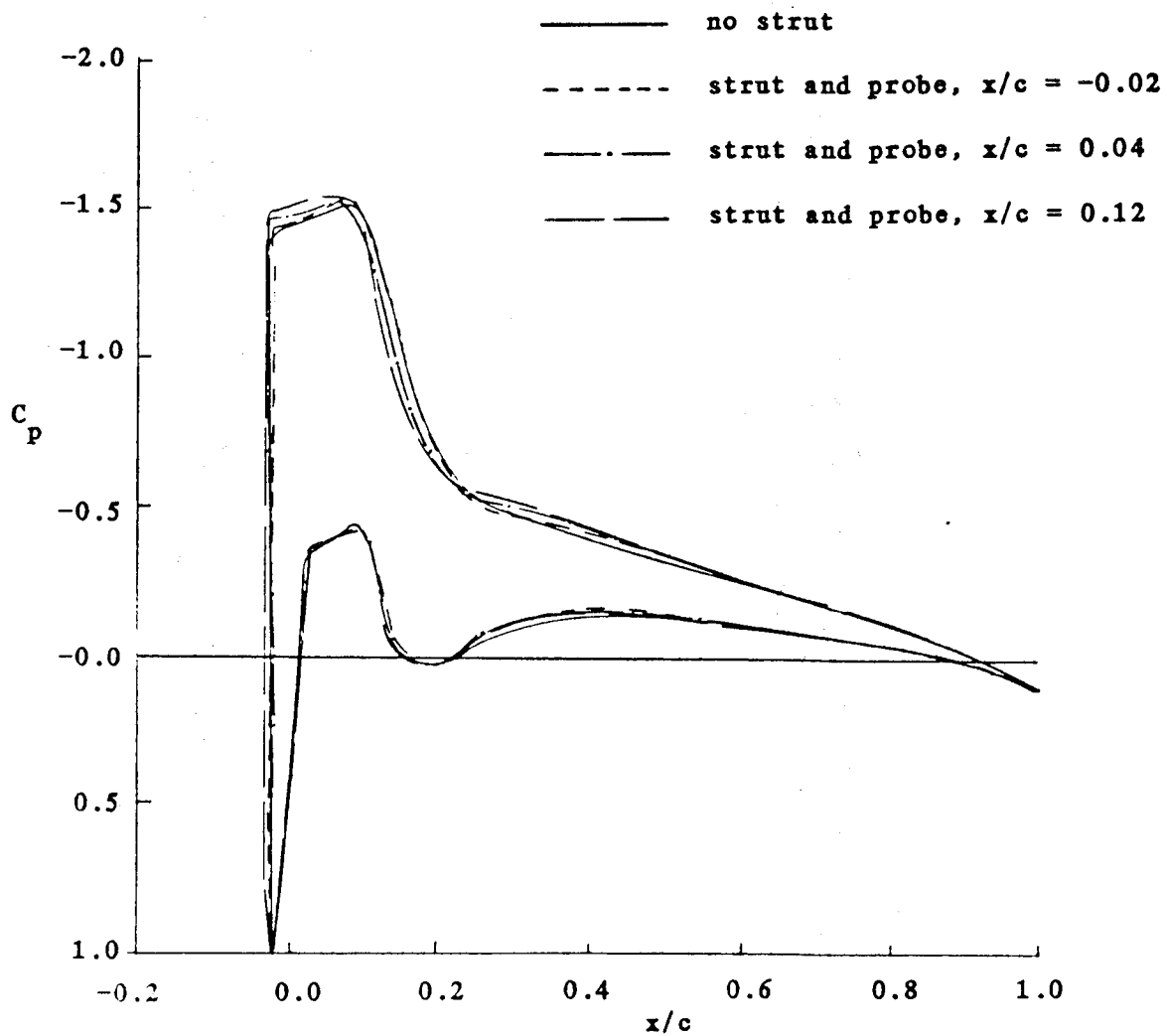
Figure 16.   Pressure distribution showing strut and probe
interference

NACA 0012 with glaze ice

Re = 1.5 x 10^6 M = 0.12
α = 4°
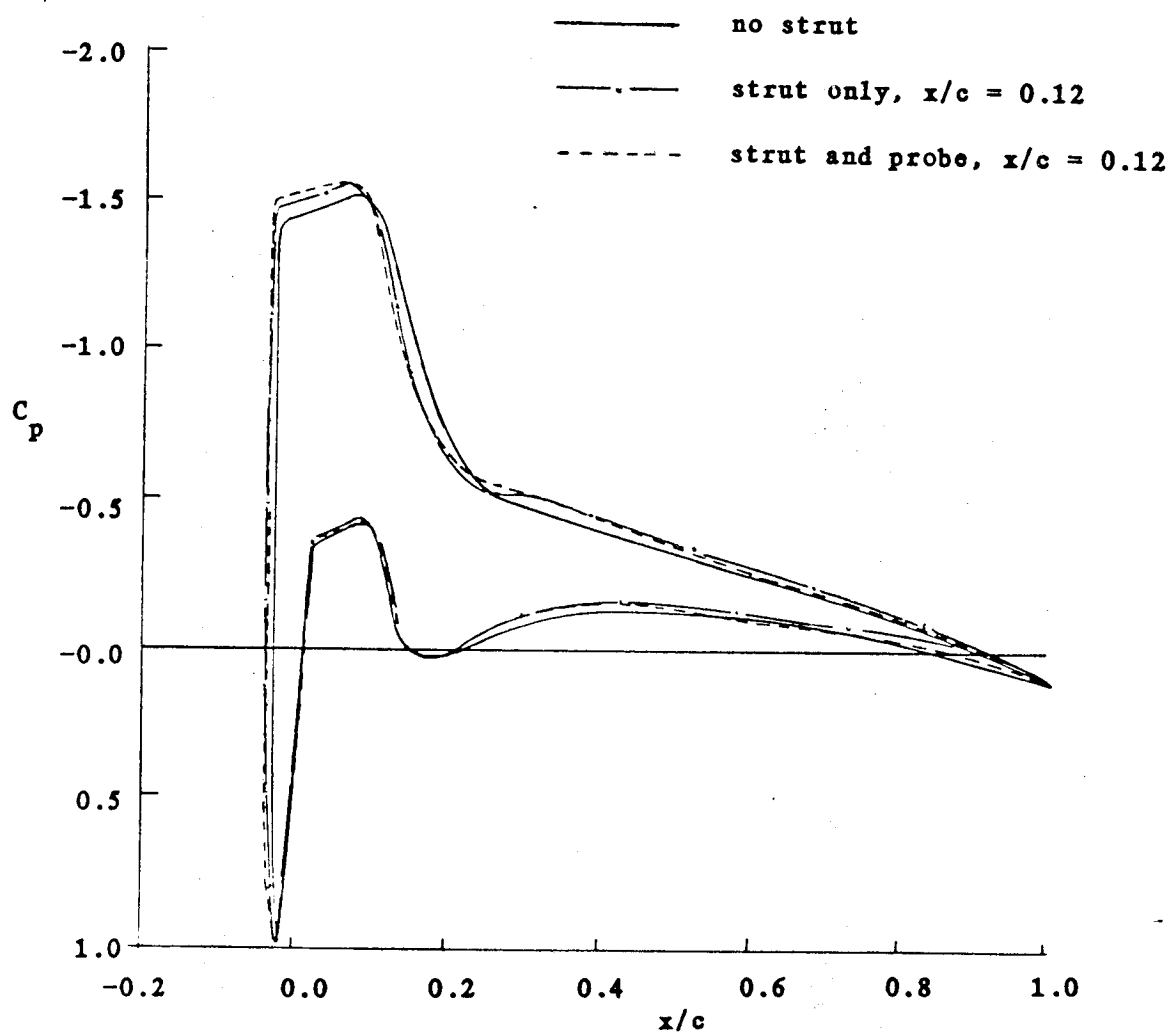
Figure 17.   Pressure distribution showing strut interference
             without probe

47

NACA 0012 with Glaze Ice

Re = 1.5 x 10^6 M = 0.12

$\alpha = 0^o$ x/c = 0.02

upper surface
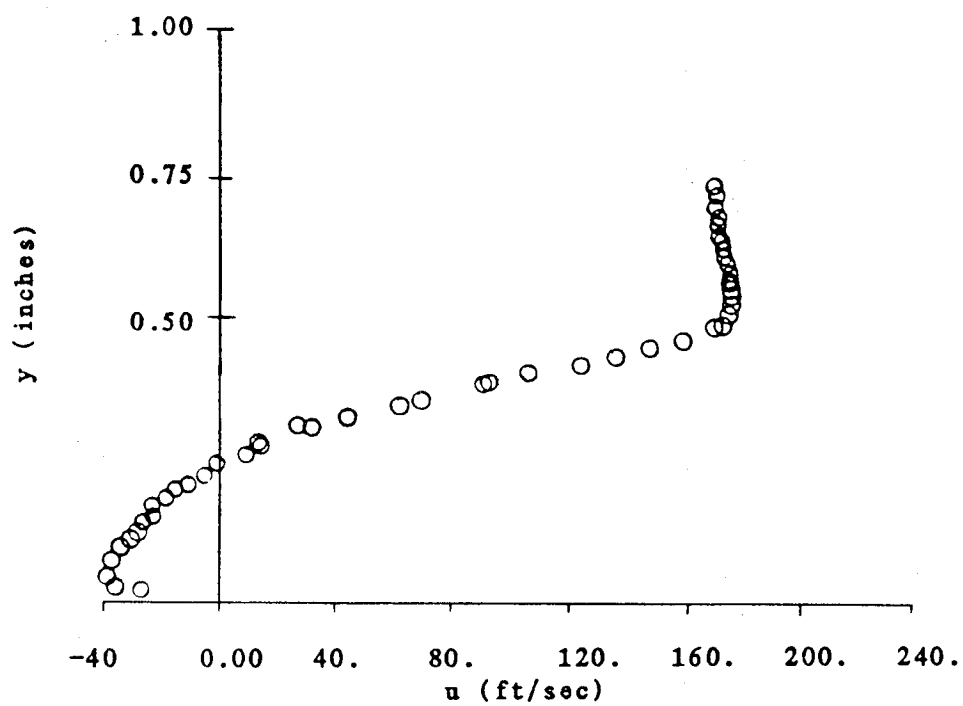
Figure 18.   Measured velocity profile showing flow reversal
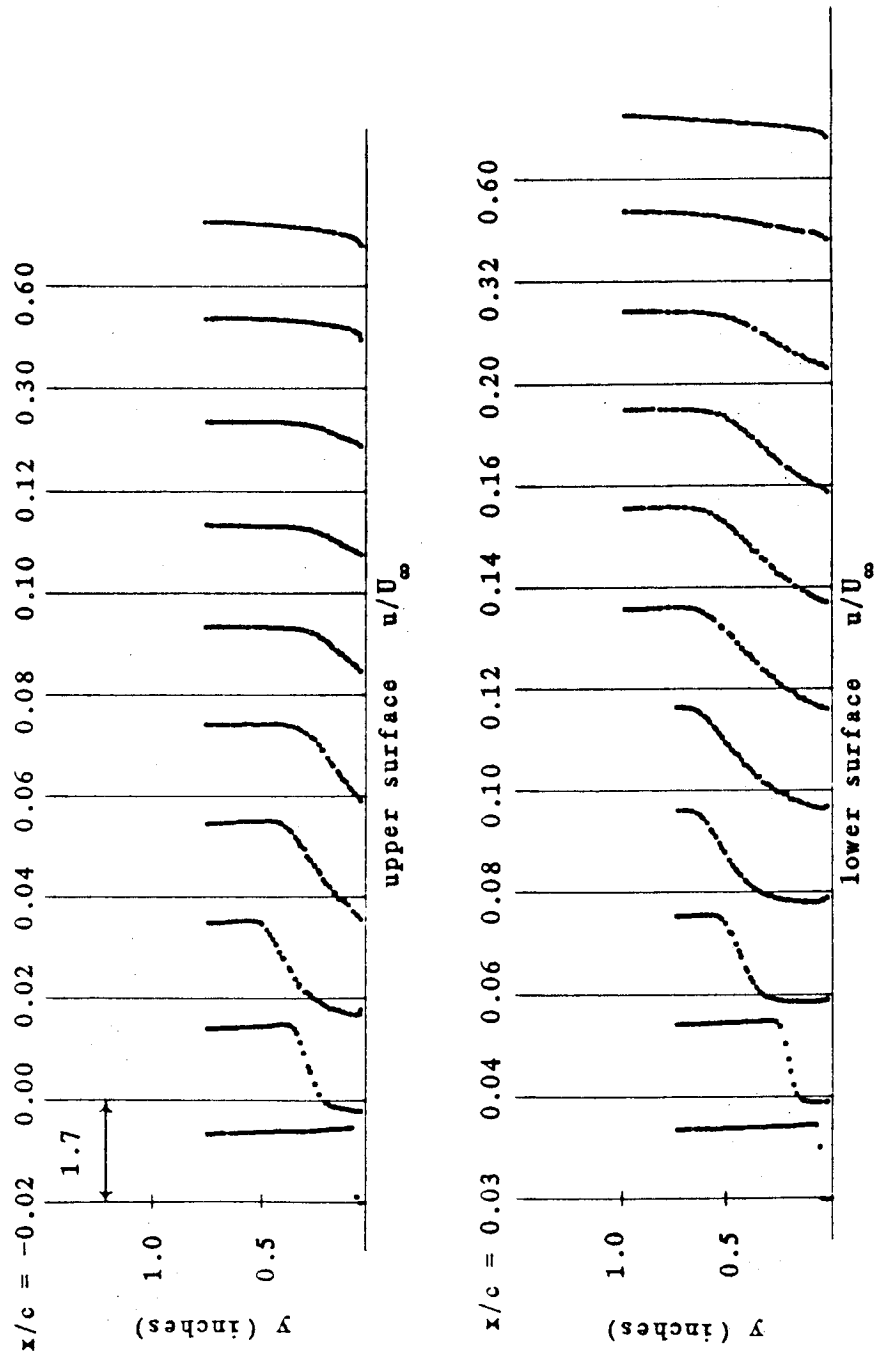
Figure 19. Velocity profiles for $\alpha = 0^{\circ}$
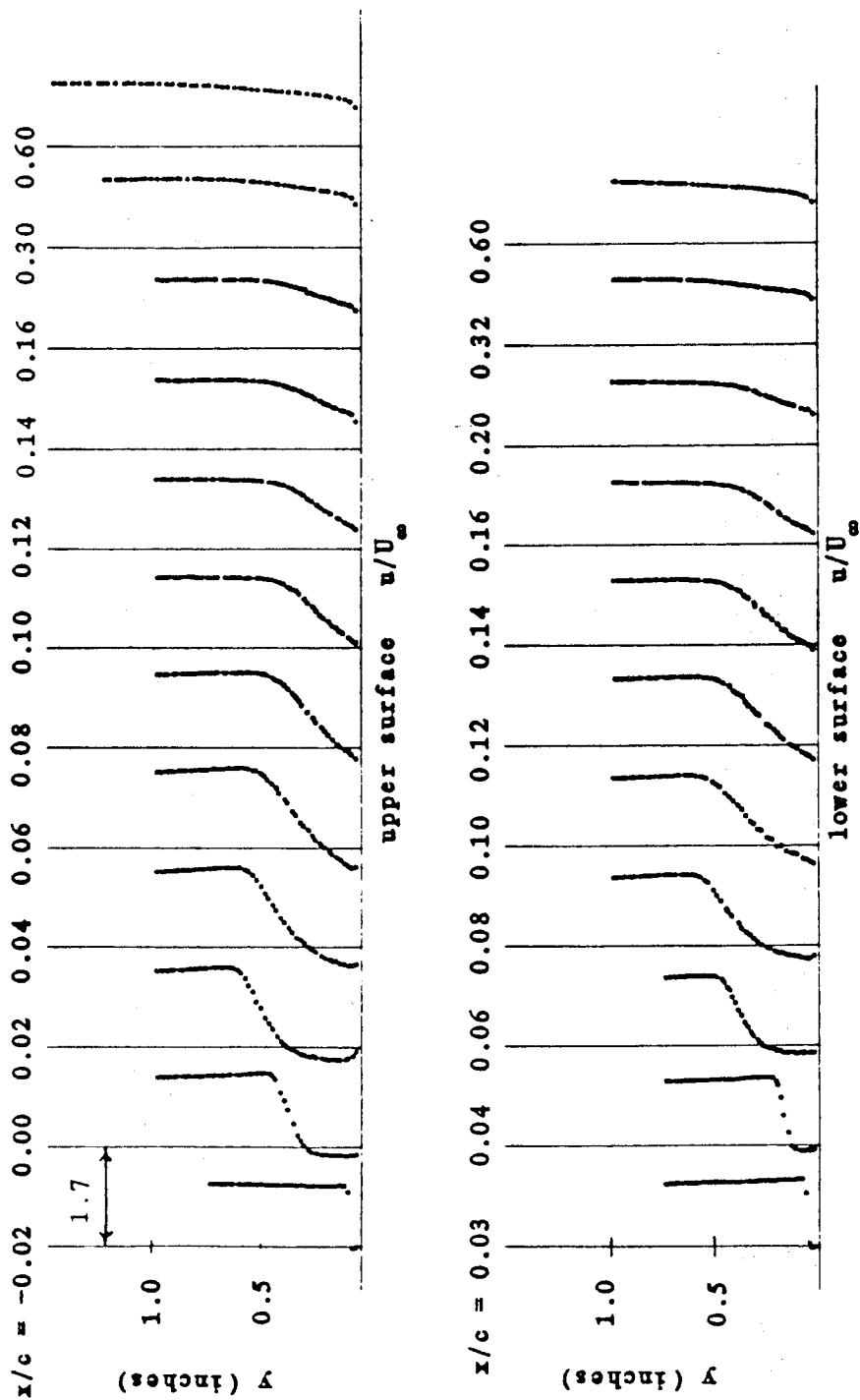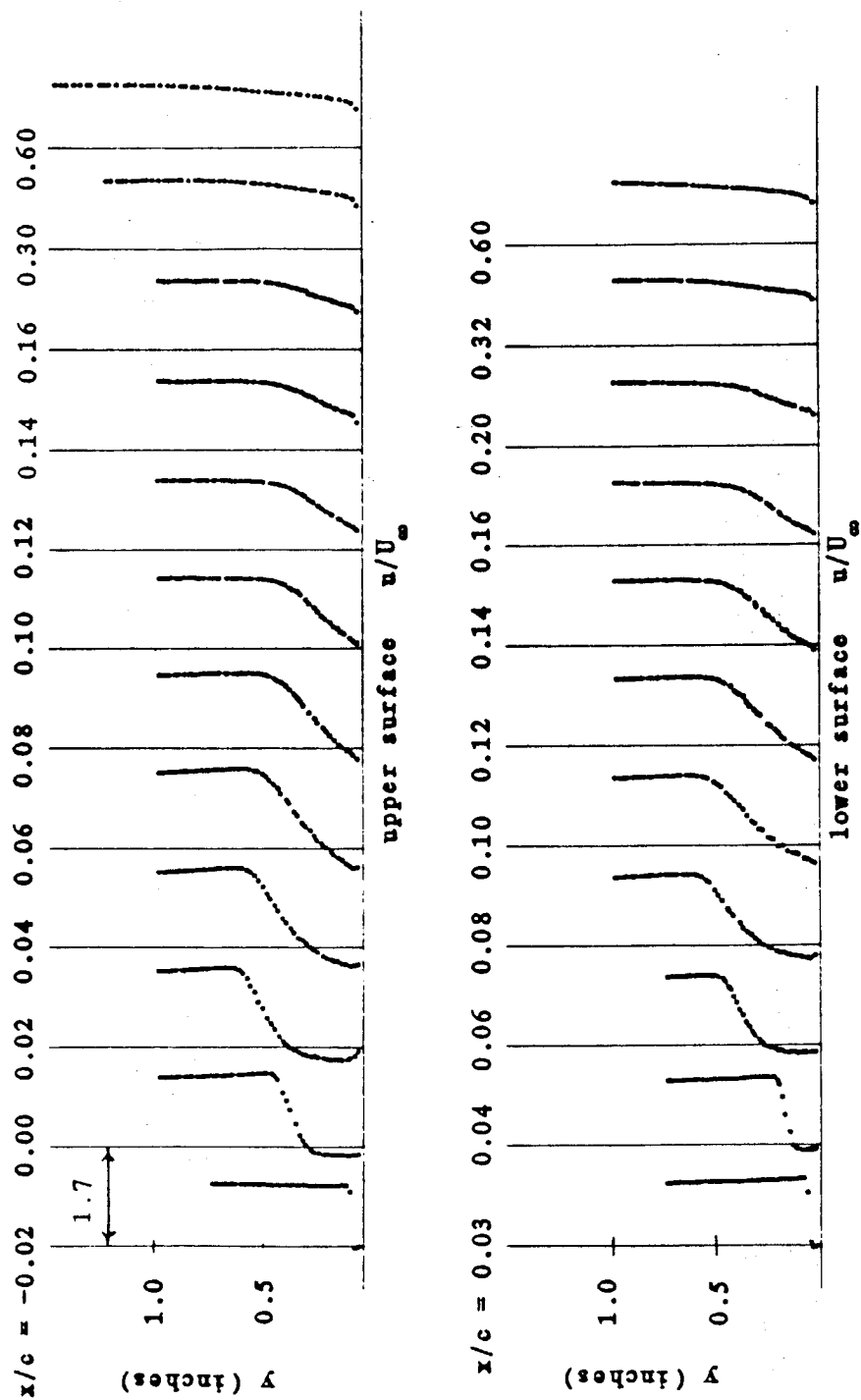
Figure 20. Velocity profiles for $\alpha = 2^{\circ}$

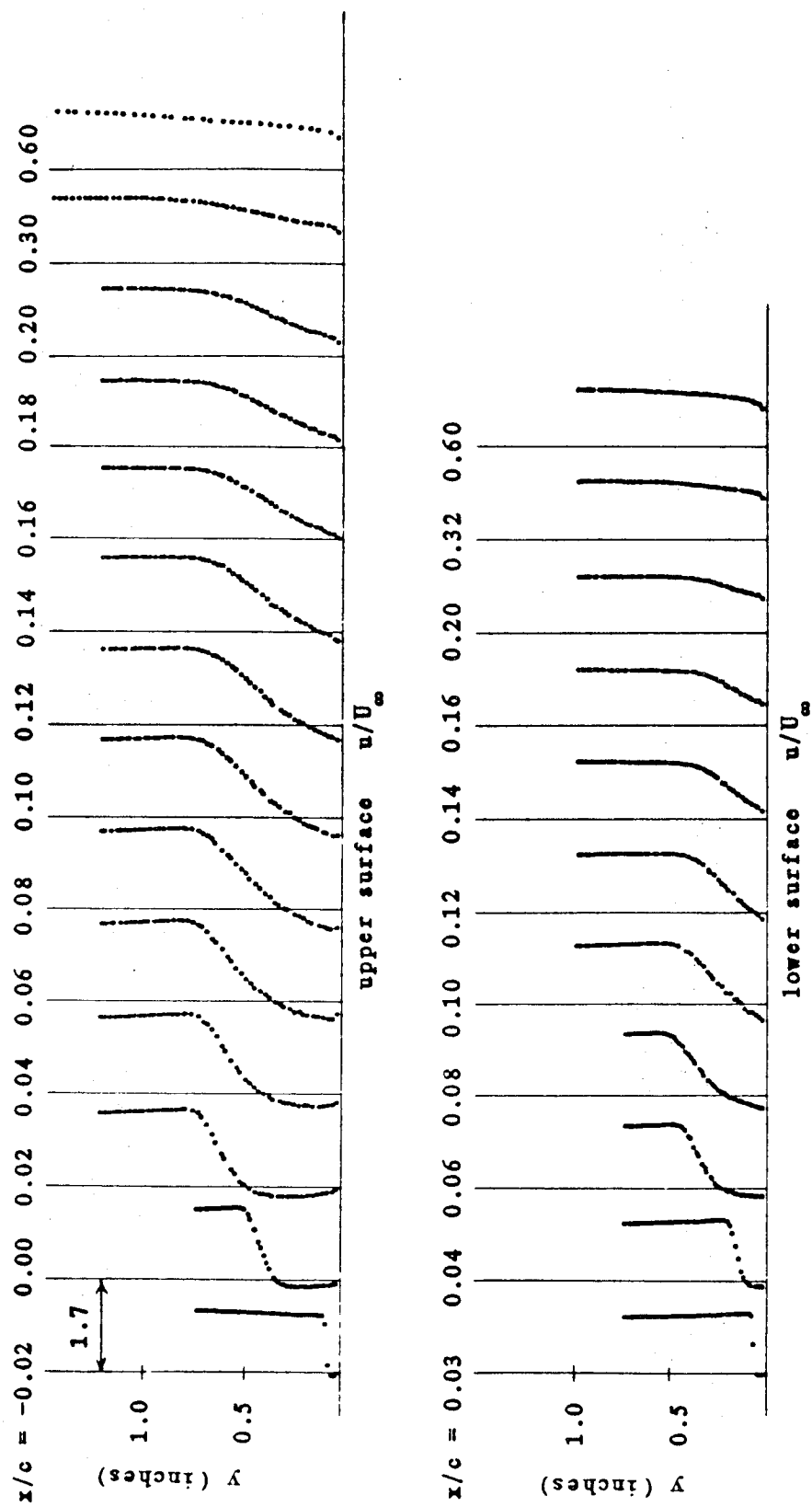Figure 20. Velocity profiles for $\alpha = 2^{\circ}$
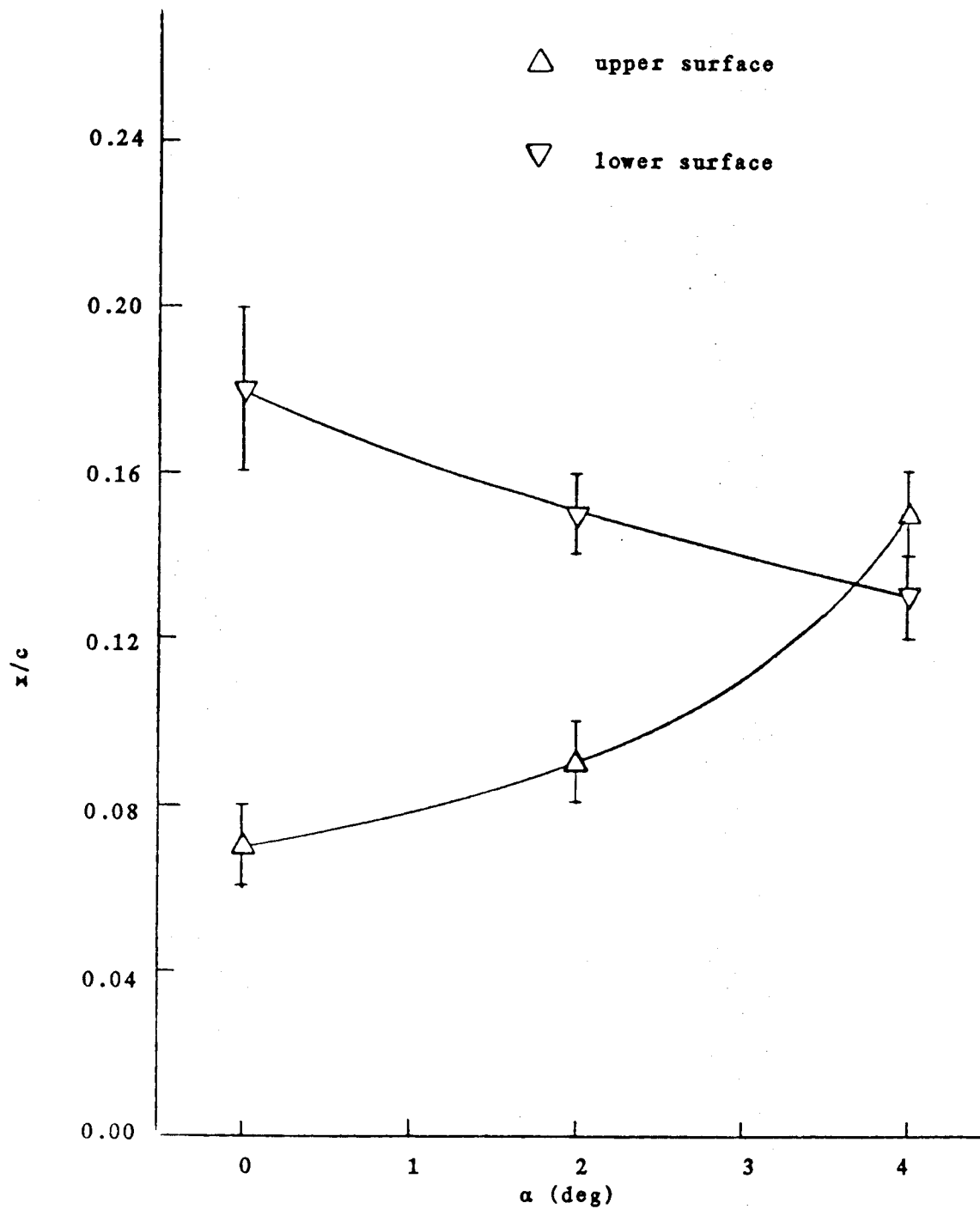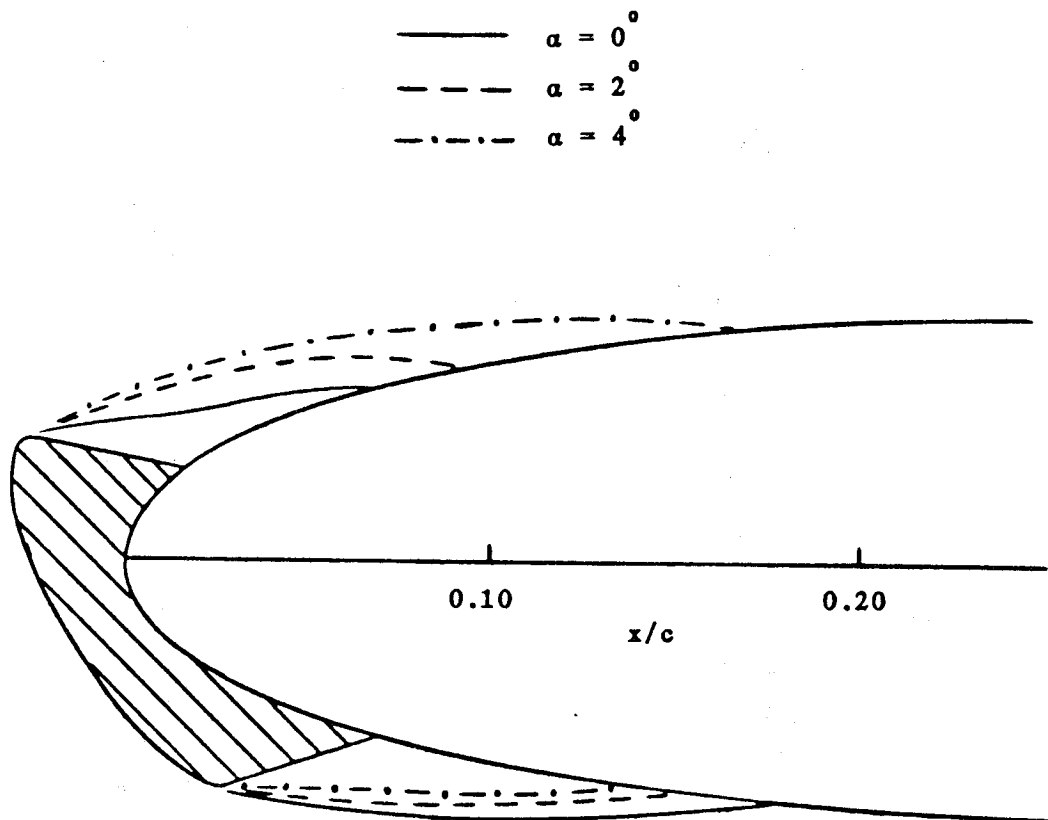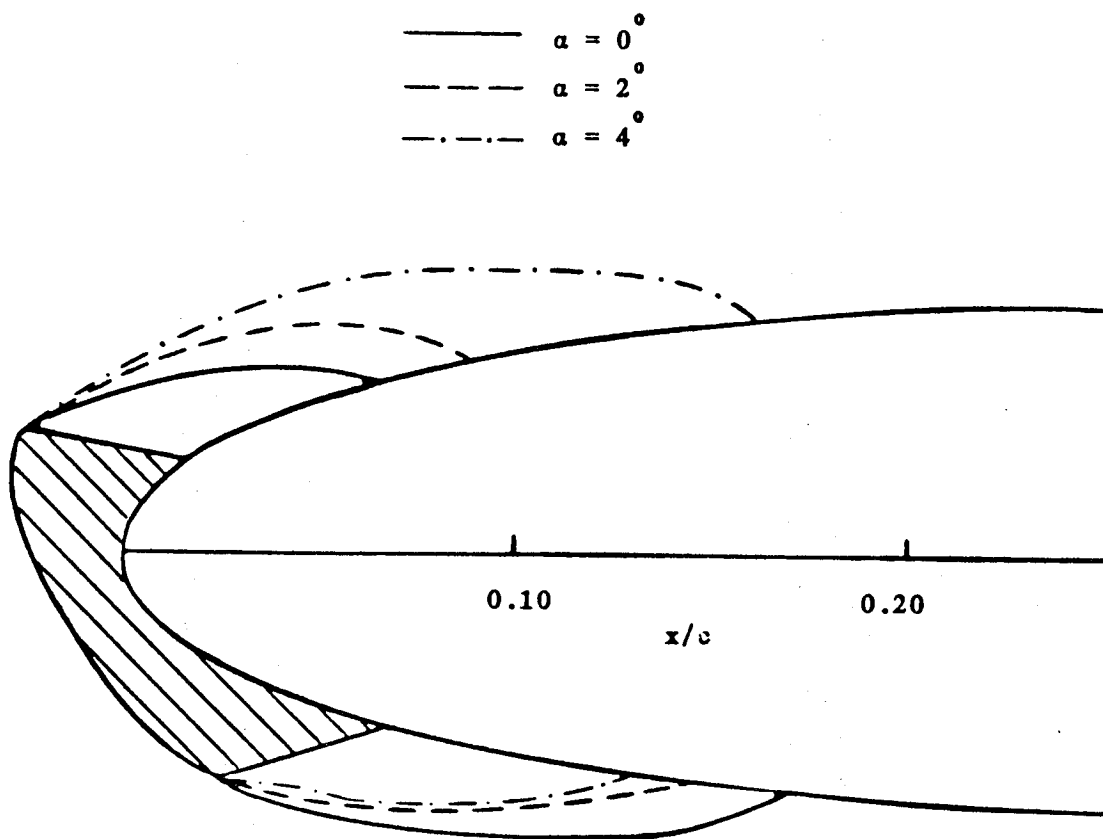
Figure 21. Velocity profiles for $\alpha = 4^\circ$

51

Figure 22. Reattachment point for NACA 0012 airfoil
with ice

Figure 23. Stagnation streamlines

NACA 0012 with Glaze Ice

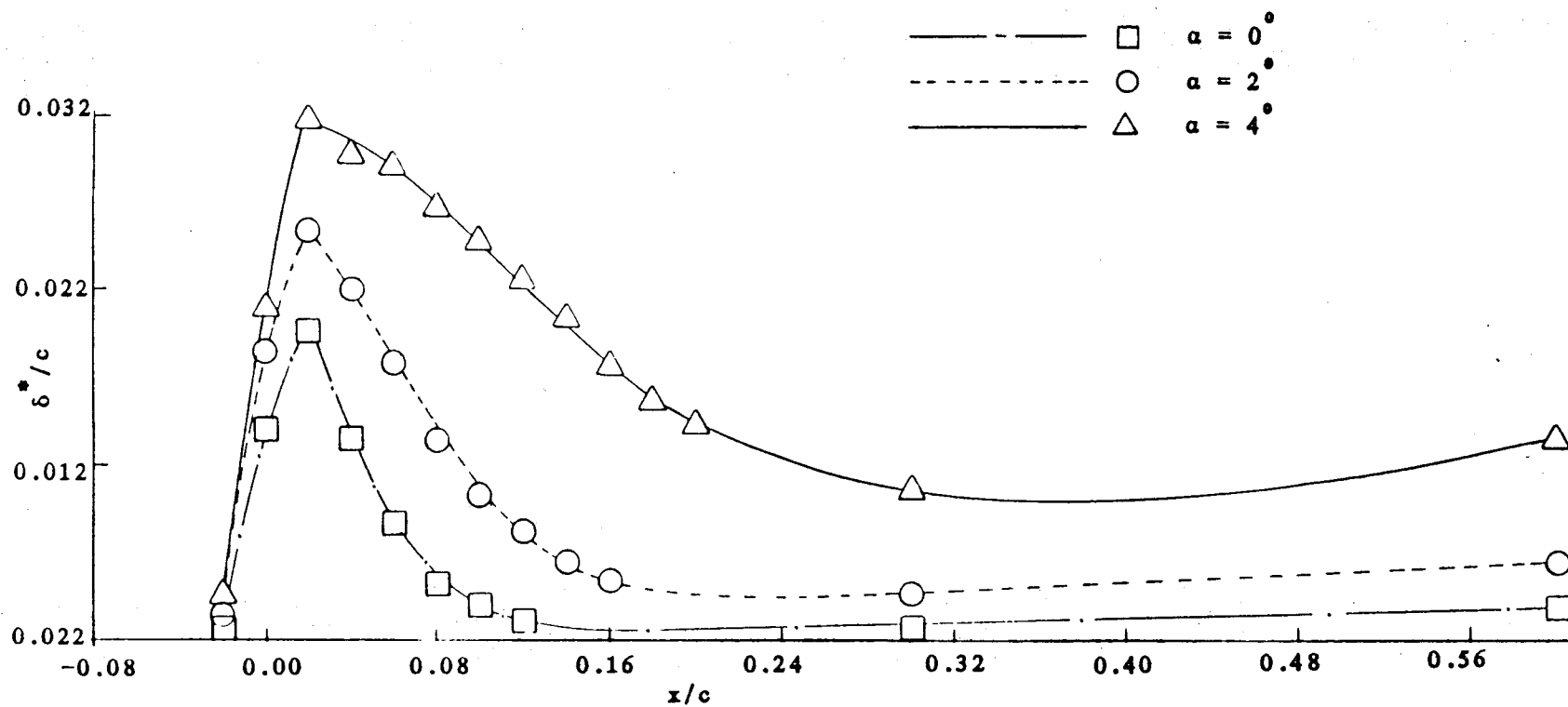Re = 1.5 x 10^6 M = 0.12

Figure 24. Separation streamlines

Figure 25. Displacement thickness over upper surface

55
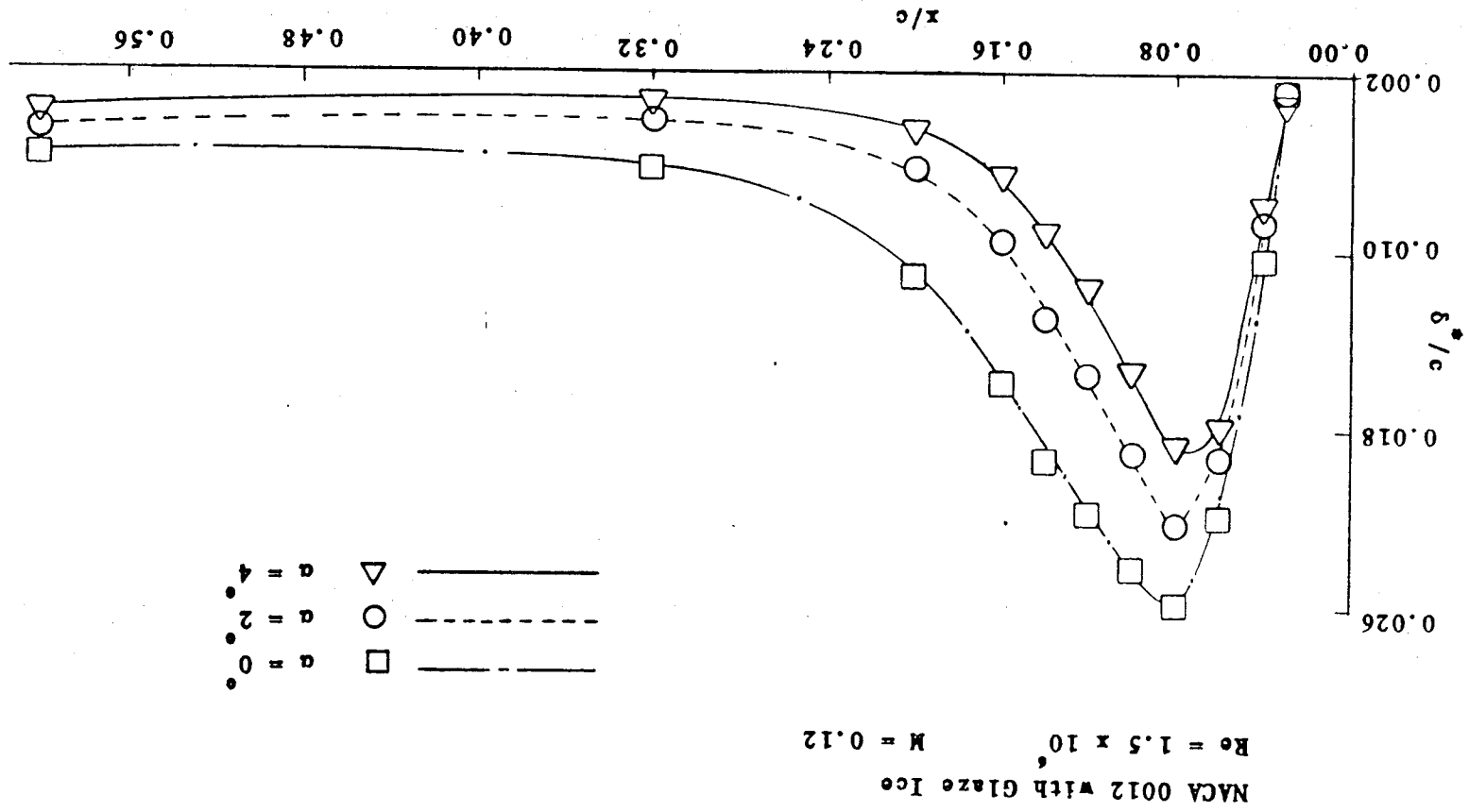
Figure 26.   Displacement thickness over lower surface

NACA 0012 with Glaze Ice

Re = 1.5 x 10⁶   M = 0.12

□   α = 0°
○   α = 2°
▽   α = 4°

x/c

δ*/c

56

NACA 0012 with Glaze Ice

Re = 1.5 x 10^{6}   M = 0.12
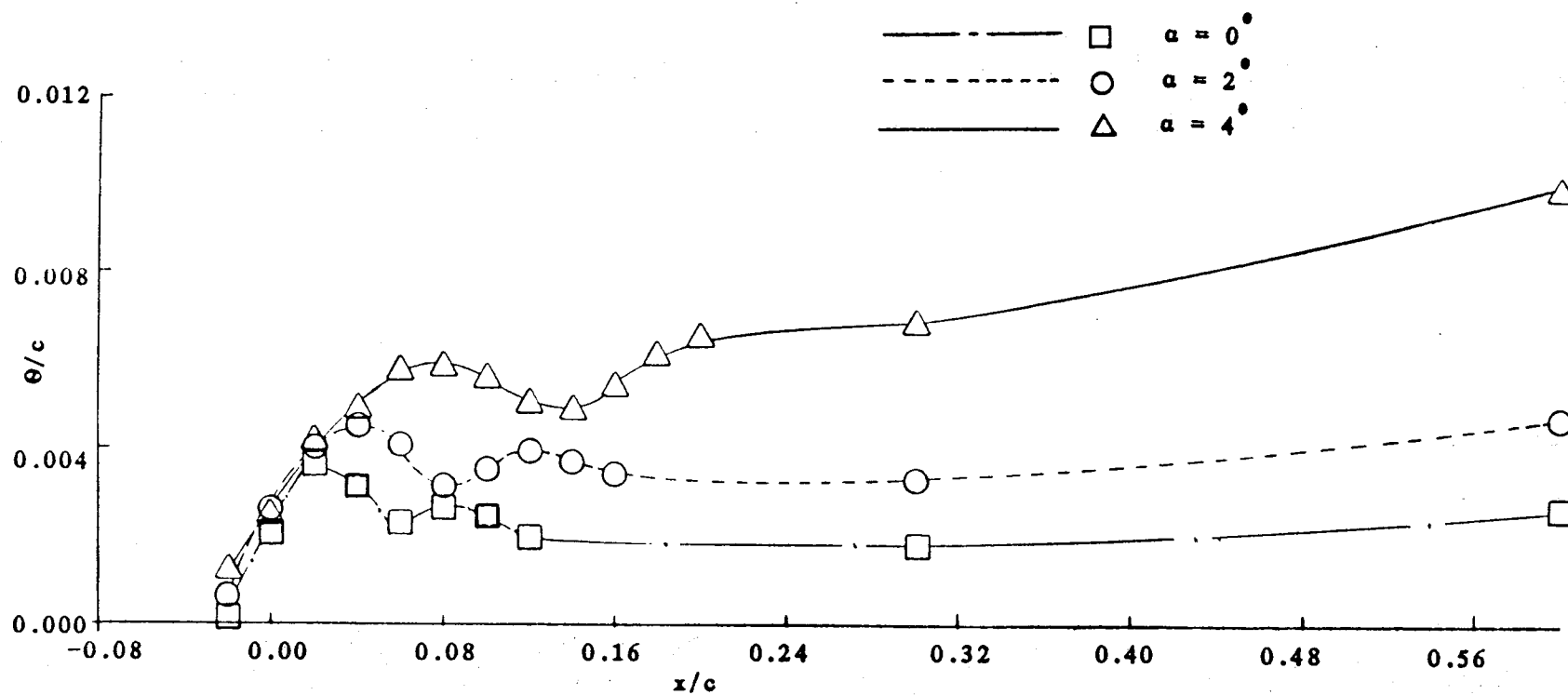
Figure 27. Momentum thickness over upper surface
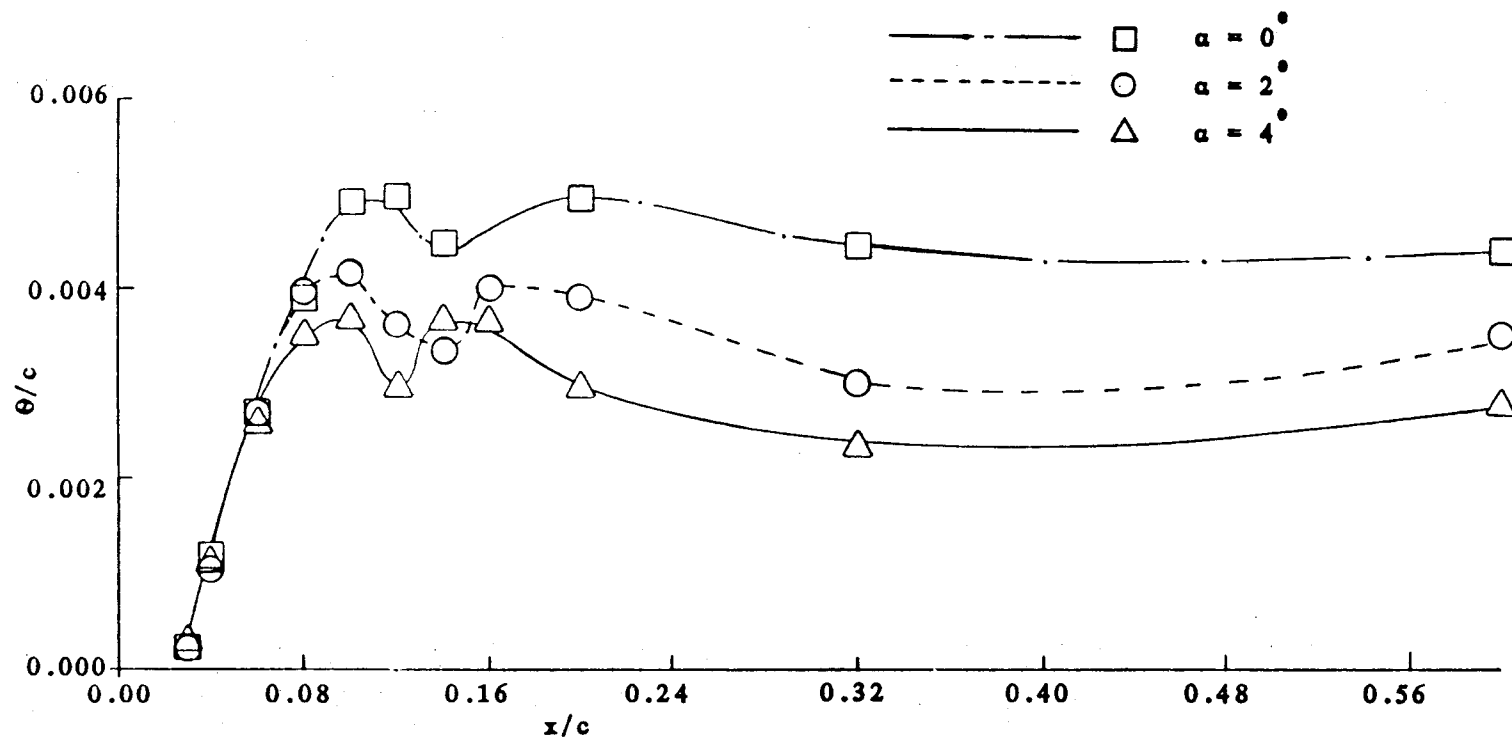
Figure 28. Momentum thickness over lower surface

58

smooth ice   X   ice with roughness, k/c = 0.0011

NACA 0012 with Glaze Ice

Re = 1.5 x 10^6 M = 0.12
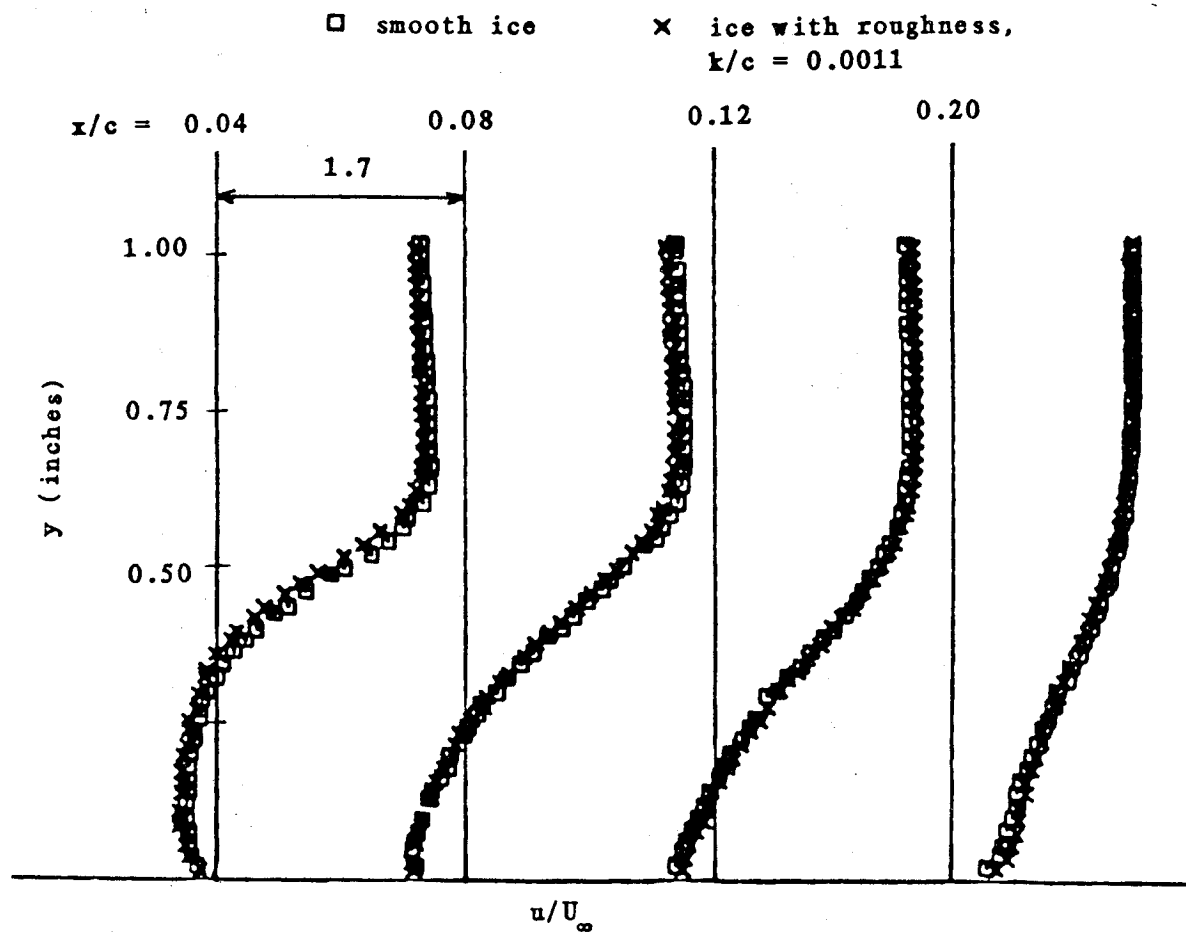
α = 4°

Figure 29.   Measured velocity profiles in upper-surface bubble with and without surface roughness at α = 4

59

APPENDIX

HOT-WIRE/FILM ANEMOMETRY

Hot films and hot wires are small resistance elements designed to measure the mass flow rate of a fluid. The sensor element is usually a fine wire supported between two posts, or a thin metallic film deposited on a quartz rod. Hot wires are usually made out of platinum or tungsten, and are very small, typically 0.0001 inches in diameter [24]. This gives the hot wire an advantage over the hot film in frequency response, signal to noise ratio, and reduced flow interference. The main advantage of the hot film is its durability. The diameter of hot films (0.001 to 0.006 inches) is large enough to mount more than one sensor element on the quartz cylinder. This allows double split and triple split films to be produced which can determine flow angularity as well as magnitude (figure 30). Double split films can determine flow angles only to $\Theta = +/- 90^{o}$. The triple split film can completely determine the flow angle but is considerably more complicated to use.

PRINCIPLE OF OPERATION

Hot-film and hot-wire systems measure the cooling of the sensor by a fluid passing across it. The sensor element is heated and held at an elevated temperature using a Wheatstone bridge circuit as shown in figure 31. The fluid flowing past the sensor cools the element, causing the resistance of the sensor to drop, thus creating an electrical imbalance in the bridge. The electrical energy required to keep the bridge balanced, i.e. to keep the element at its operating temperature, is a measure of the mass flow rate of the fluid. The heat transfer around an infinite cylinder is given approximately by King's Law as a function of mass flow:

$$Q = \frac{E^2}{R_w} = (A + B \ (\rho U)^{0.5}) \ (T_s - T_e) \qquad (11)$$

The constants A and B are dependent on the particular fluid and, for air, are considered invariant with temperature [25].

Notice that the heat transfer is a linear function of the temperature difference between the hot film and fluid. This is important since this temperature difference is not always the same during the calibration and during the actual data acquisition. However, for a given mass flow, a ratio of the heat transfer from the calibration, to the heat transfer from the run data, gives a simple relation for the

temperature compensation. This assumes that the sensor temperature (and resistance) is constant.

$$E_{corr} = \left[\frac{T_s - T_{cal}}{T_s - T_e} \right]^{0.5} E \qquad (12)$$

For split films, the heat transfer is actually the sum of the squares of the voltages from the individual sensor elements. However, the same temperature correction can be applied to each sensor voltage by virtue of the fact that the local heat transfer coefficient around a cylinder is a function of Reynolds number and position, but not a function of the temperature [26].

After the correct voltage has been obtained, the user then obtains the corresponding mass flow from a calibration curve. In other words, for the voltage output, the mass flow rates are equal for the calibration conditions and the run conditions.

$$\rho U = \rho_{cal} U_{ind} \qquad (13)$$

If the density was the same during the run as it was during the acquisition, this would directly yield the velocity. If the density has changed, a rearrangement of the terms, and use of the perfect gas law, gives a simple density correction.

$$U = \frac{\rho_{cal} \, U_{ind}}{\rho} = \frac{p_{cal} \, T}{T_{cal} \, p} \quad U_{ind} \qquad (14)$$

The density correction applies to the velocity whether it is the total velocity, as from a single element sensor, or a velocity component from a multiple element sensor. The method for obtaining the indicated velocity components from the calibration is presented in the next section.

CALIBRATION

The calibration of cylindrical single element sensors is the same for wires and films. The method changes only if a multi-element hot film is used. Therefore, the calibration scheme for only the single film and the double-split film is discussed here.

For single films the objective is simple. Place the film in a constant velocity field of known magnitude and read the voltage output. This is done for several velocities to produce a calibration curve. Usually, the data is corrected to a reference condition, and then all run data is corrected to the same condition. However, one correction can be avoided by using the calibration conditions as the reference. Referring to King's Law, the calibration curve of velocity versus voltage can be fit using a fourth order polynomial. Figure 32 shows a typical calibration curve for a hot film.

The process becomes more involved for a split film. Now the angle as well as the magnitude of the velocity must be varied. The curve fitting procedure is also made more difficult.

The completed calibration used here consists of five curve fits. The first curve fit comes from the $\Theta = 0^{\circ}$ data. K is the ratio of the voltages from the front side of the split film to the back side, at $\Theta = 0^{\circ}$, and should theoretically be constant and equal to one. Manufacturing defects create slight imbalances between the two channels that can accounted for using K as a function of the velocity, or as a function of the square of the sums of the voltages. In this study, K is fit into a polynomial as a function of the square of the sums of the voltages.

$$K = f(E_1 + E_1)^2 \qquad (15)$$

The next pair of curve fits come from the $\Theta = 90^{\circ}$ data points. The total velocity is fit to a function of the same argument as K, the square of the sums of the voltages. Then an E_{max} term is fit as a function of the total velocity, where E_{max} is defined as

$$E_{max} = (E_1^2 - K^2 E_2^2)_{max} = f(U) \qquad (16)$$

64

This term is the maximum difference in the voltages at a particular velocity, i.e. at $\Theta = 90°$. If the flow angle is between $0°$ and $+90°$, then this pair of curve fits is used to reduce the data.

The final pair of curve fits are identical to the previous two except they come from the $\Theta = -90°$ data. This pair of curve fits are used if the flow angle is between $0°$ and $-90°$.

In the reduction, the same procedure is followed. The voltages are first corrected for temperature differences between calibration and acquisition. Then a value for K is obtained through the first curve fit. The general direction of the flow is determined by examining the relative magnitudes of E_1 and $K E_2$. Then the appropriate pair of curve fits, depending on the sign of the flow angle, are used to obtain values for U and E_{max}. The following sine function is used to find the flow angle [18].

$$\sin \Theta = \frac{(E_1^2 - K^2 E_2^2)}{E_{max}} \qquad (17)$$

Now that the flow angle is known, the velocity components can be found.

$$u = U \sin \Theta \qquad\qquad v = (U^2 - u^2)^{0.5} \qquad (19)$$

This relatively simple calibration scheme works quite well. Figure 33 shows a typical calibration with data taken at several angles

as well as 0° and $+/- 90^o$. The curve fits approximate the calibration data to a reasonable degree of accuracy.

HOT FILM PROBLEMS

Hot films have several trouble spots that must be avoided to obtain accurate velocity data. Only some of the problems outlined were encountered in this research.

All hot-wire and hot-film sensors are vulnerable to contamination. Dust and dirt collect on the sensor element and change the heat-transfer characteristics of the sensor. This introduces an error into the calibration that may be an offset as well as a change in the sensitivity of the sensor. Figure 34 shows a plot of the voltage squared versus the square root of the velocity, for a single element hot film before and after probe contamination. This probe was run for several hours during the month of June in the OSU 3x5 wind tunnel. The effect of the contamination was to lower the zero-flow voltage and increase the sensitivity of the sensor. Sensor contamination is a function of the amount of contaminants in the air, i.e. dust, pollen, bugs, etc. Thus it is felt that the contamination is a function of the time of year, for an open-return tunnel. Hot films can be cleaned with acetone, but they do not always return to the original calibration. Heating the sensor to a temperature well above its normal operating temperature will burn some of the contamination off, and may be a good

66

method for cleaning the probe. In the experiments with the split film, no noticeable contamination was observed.

Another problem with all hot-film/wire sensors arises when data are taken near a solid boundary. Heat transfer from the probe to the wall can make the velocity appear artificially high [27]. The NACA 0012 model used for these tests was made out of wood with a fiberglass skin, and was assumed to be an insulated surface with no heat transfer difficulties.

Proper calibration of the sensors can sometimes be a problem. A simple way to calibrate a hot film is to place the sensor tip in a small jet of air. The problem arises because the entire support structure is left out of the jet, and the corresponding interference effects are left out of the calibration. If the probe is calibrated and operated in an end flow configuration ($\theta = 0^o$), the error in velocity is roughly two to three percent and can be corrected. In cross flow however, the errors are much larger (10-17 percent) and are inconsistent. The error is also very sensitive to minute geometry details (weld points, etc.). Figure 35 shows the variation of voltage output with probe angle in a free air jet from a 0.25 inch diameter exit. The probe used here produced an output that was not even symmetric about $\theta = 0^o$. With such wide variations in output, it would be impossible to calibrate a split film for angular dependence with any accuracy in such a device. A calibration flow large enough to envelope the support prongs of the probe should be used to obtain accurate

calibrations. The calibrator used for this study was a four inch diameter, ejector driven tunnel. Even with a proper calibration, there are large differences between end flow and cross flow calibrations (figure 36). For this reason, single films should be calibrated in the same configuration they will be used in for accurate results.

The interference effects may be a problem even if a good calibrator is used. This is because the calibration uses a flow with a constant velocity cross section. In this study, the probe was used in a boundary layer where the shape of the velocity profile was unknown apriori. The velocity profile was also varying rapidly. This made it nearly impossible to account for the interference effects in the calibration. This error is inherent in the present measurements.
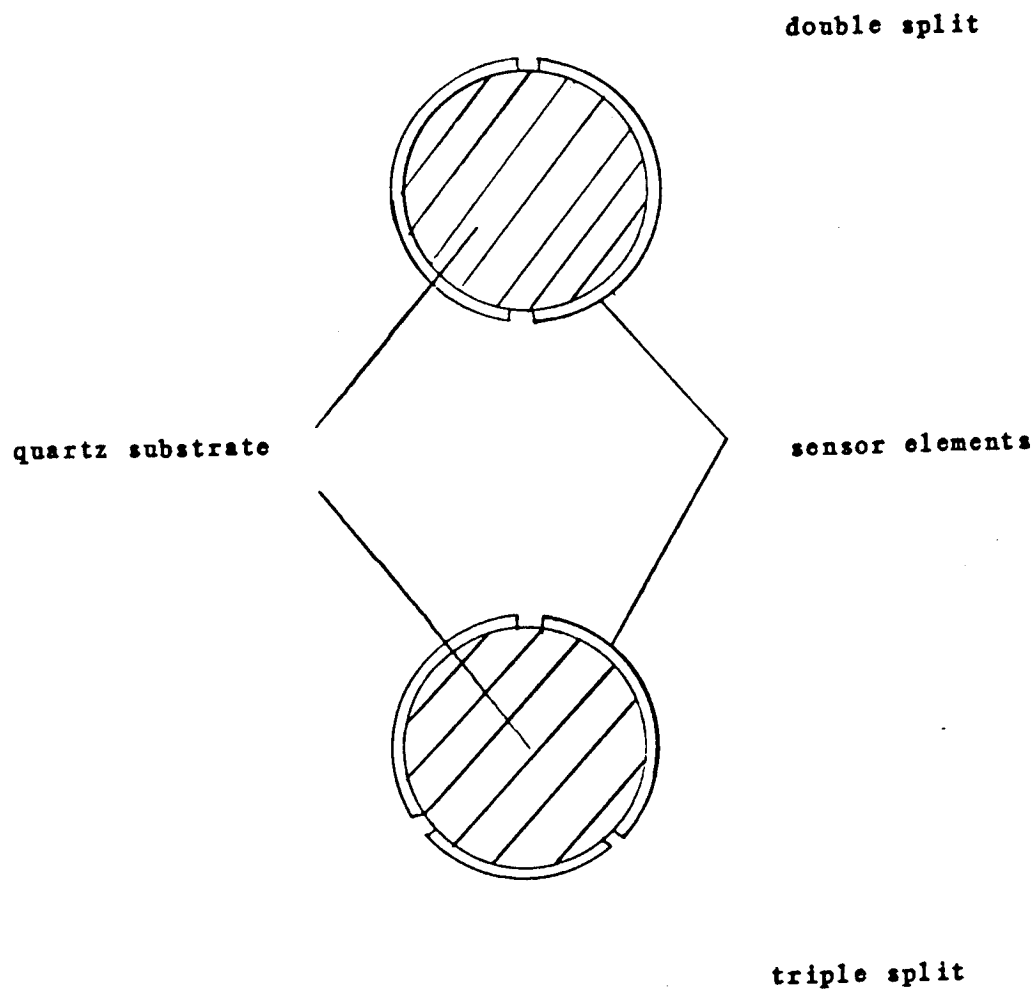
double split

quartz substrate   sensor elements

triple split

Figure 30.   Cross section of double and triple split-film
sensors

R

R

operational
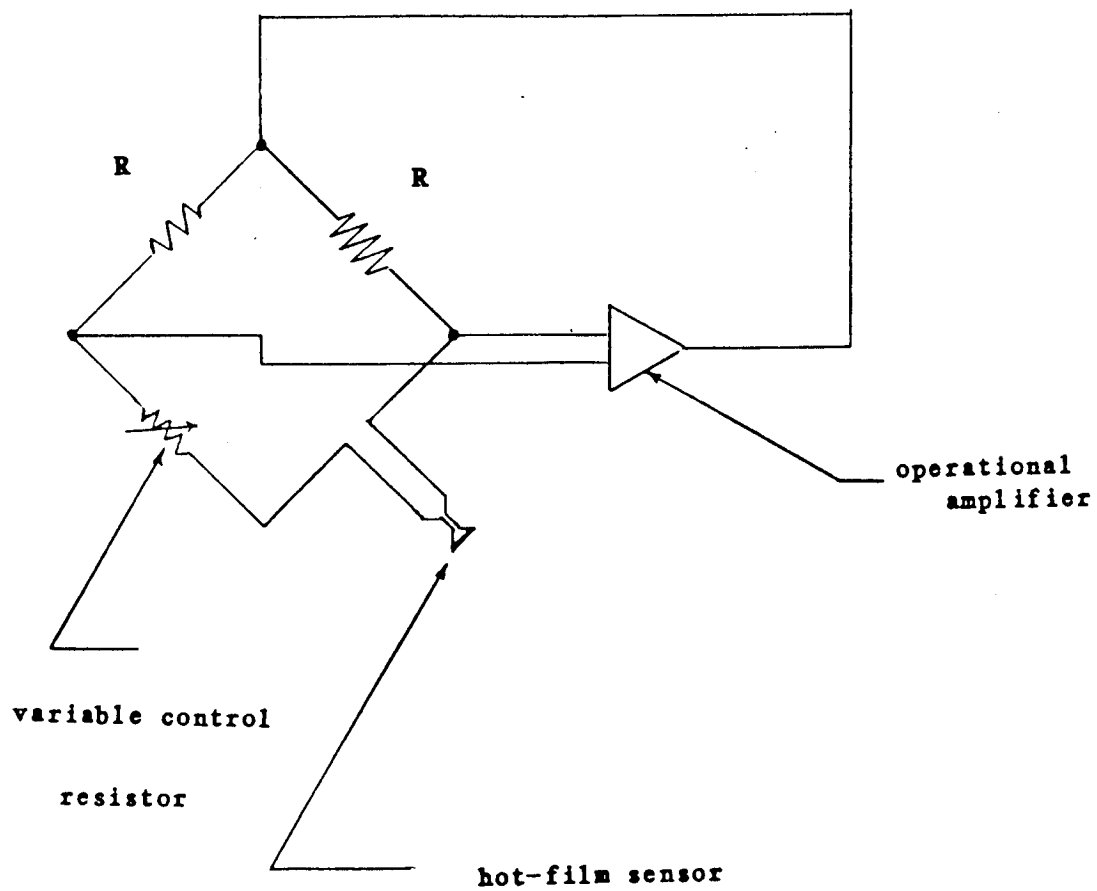amplifier

variable control

resistor

hot-film sensor

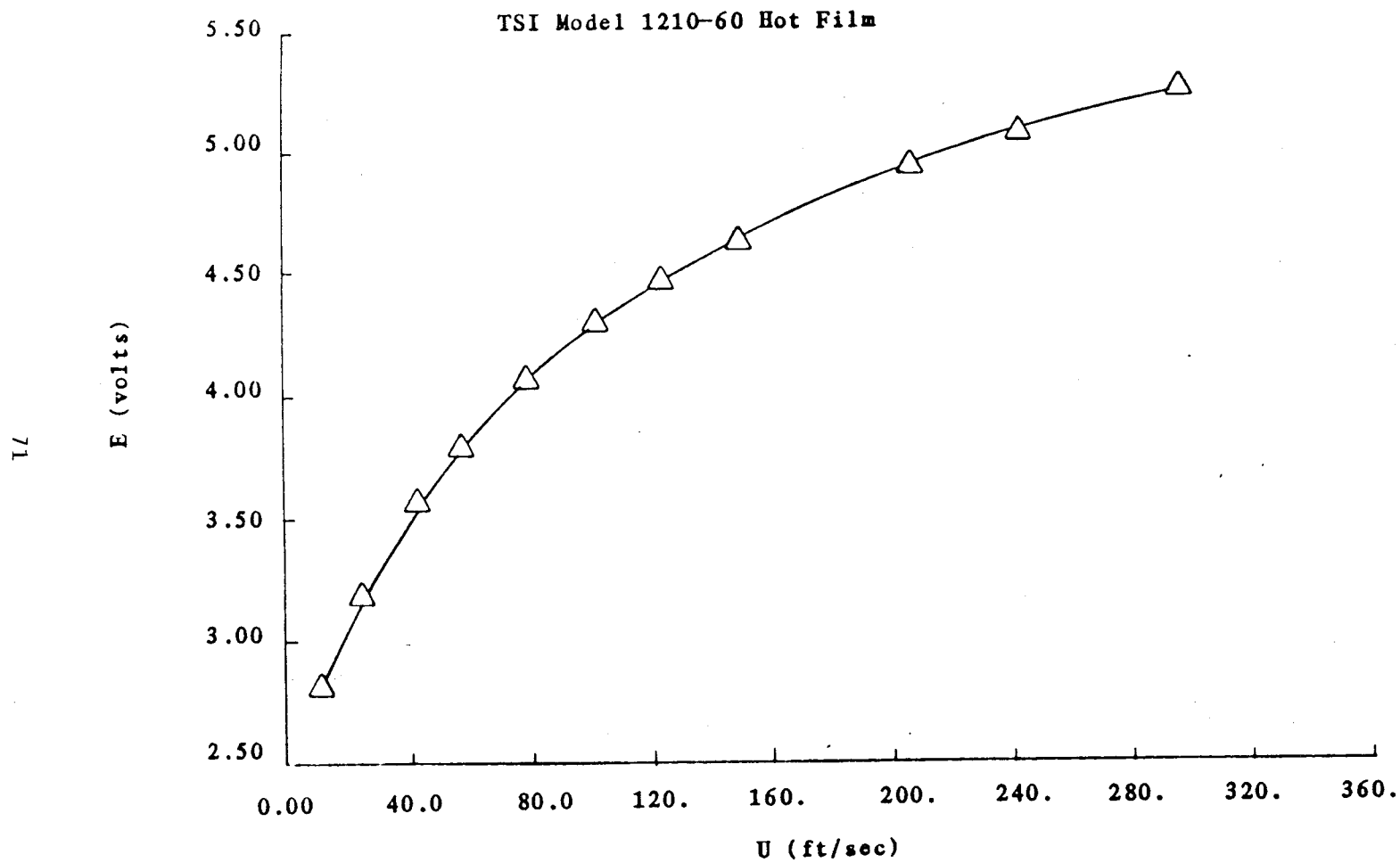Figure 31.   Schematic of Weatstone bridge

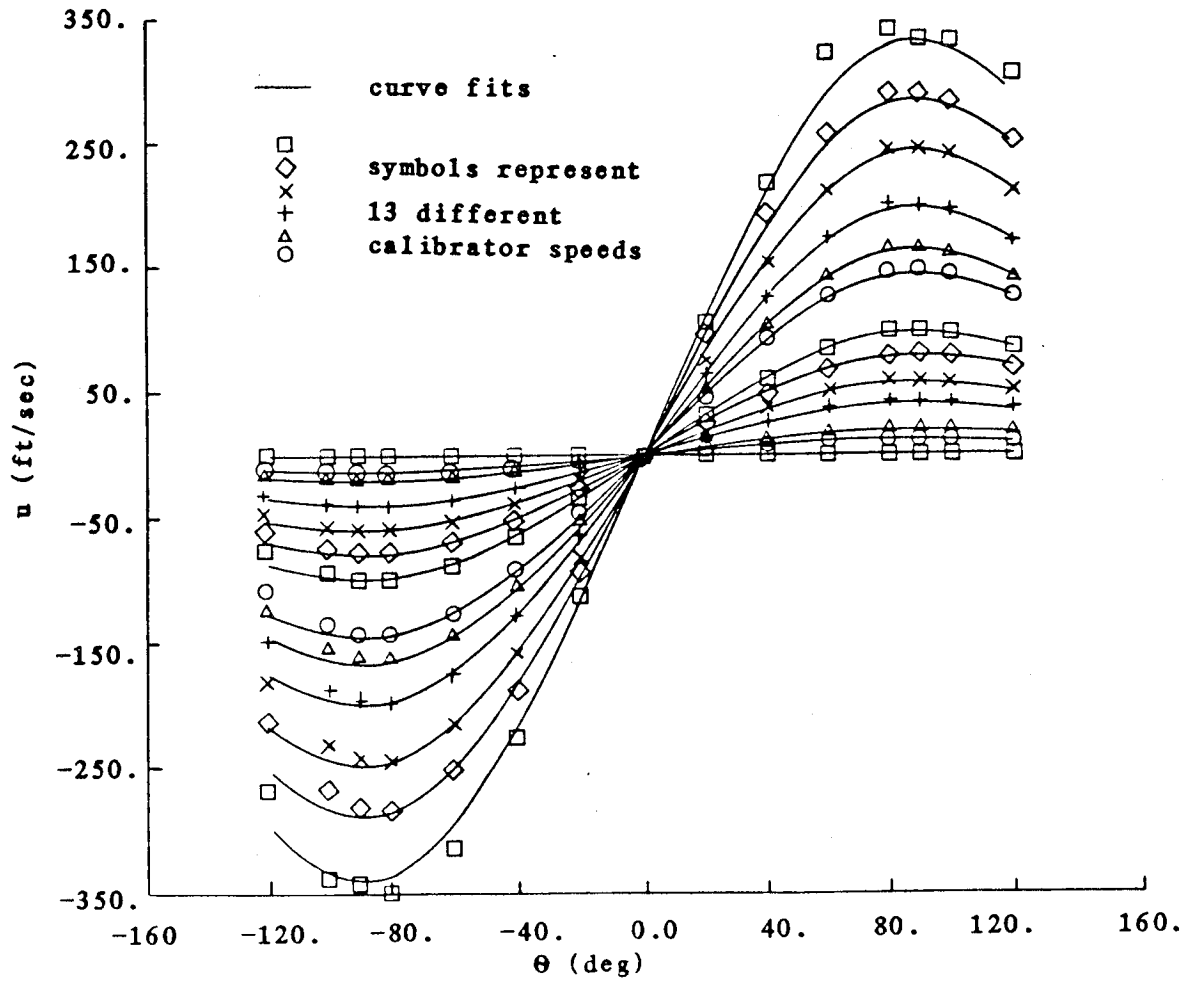Figure 32. Typical single-element hot-film calibration curve

TSI Model 1288 Split Film

Figure 33. Typical double-element hot-film calibration curve
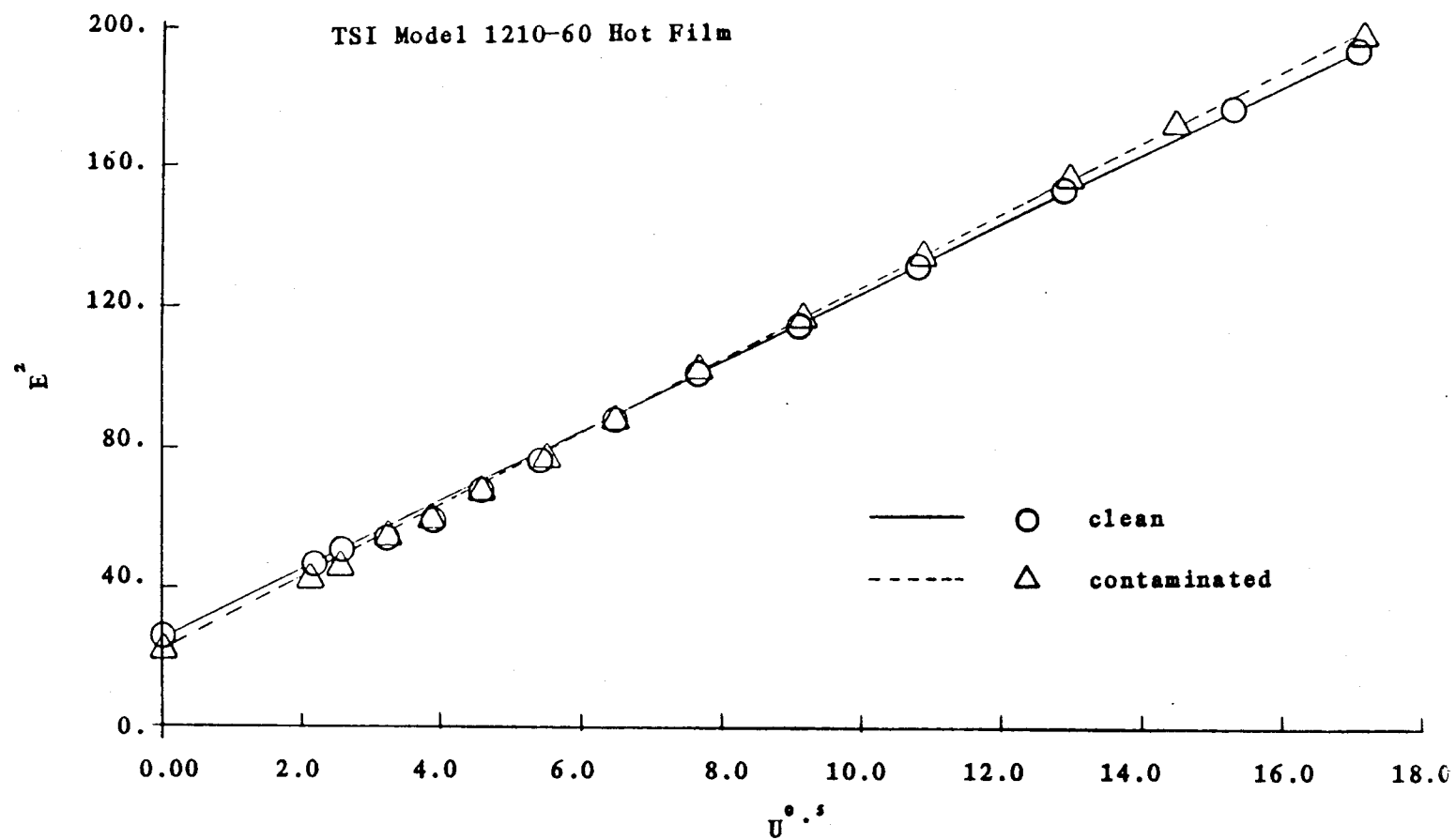
Figure 34. Contamination effects on single element hot film

TSI Model 1210-60 Hot Film

E (volts)

12.30 12.26 12.22 12.18 12.14 12.10

Θ (deg)

-90 -70 -50 -30 -10 10 30 50 70 90
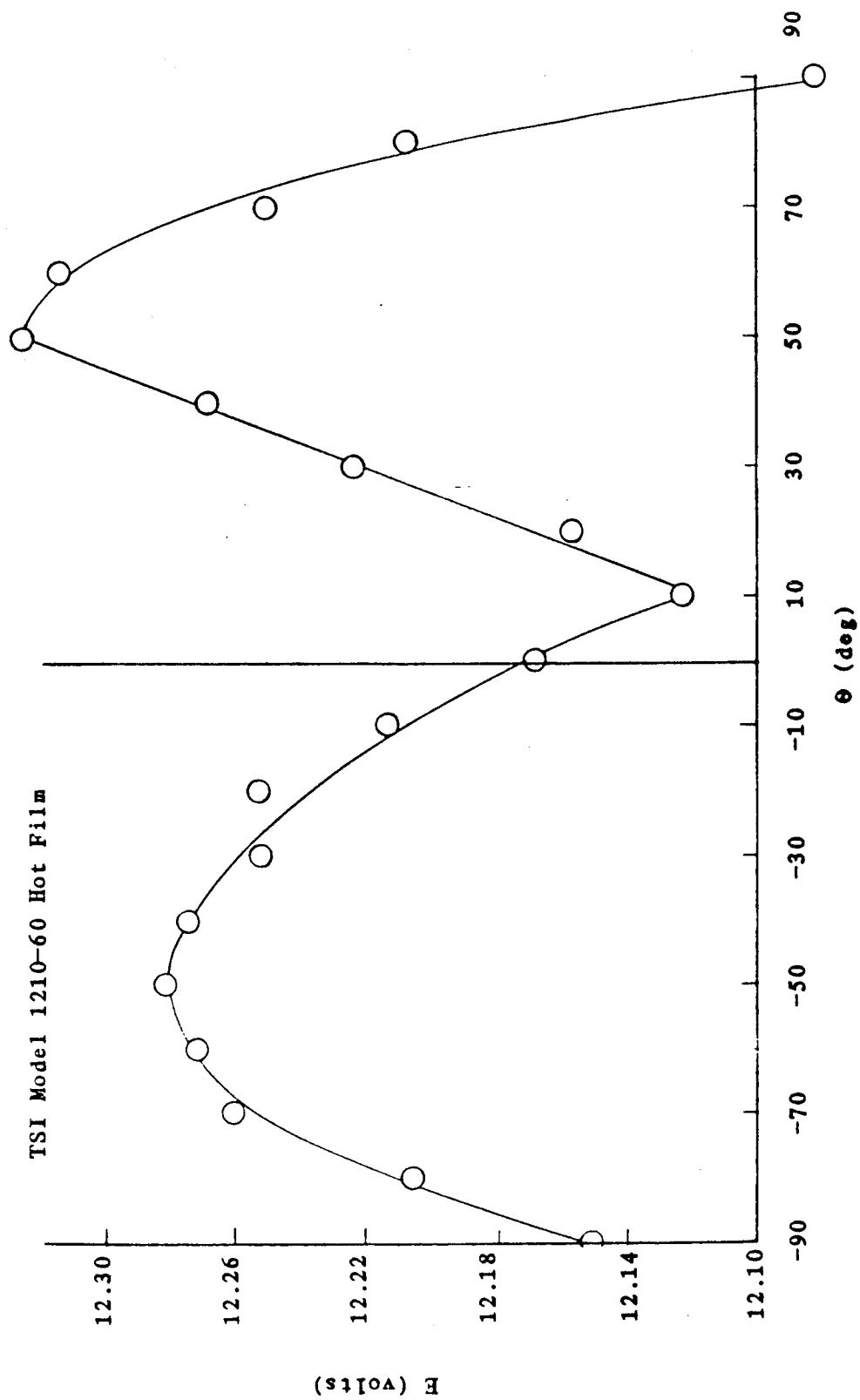
Figure 35. Variation of voltage output versus pitch angle of a single-element hot film at constant velocity
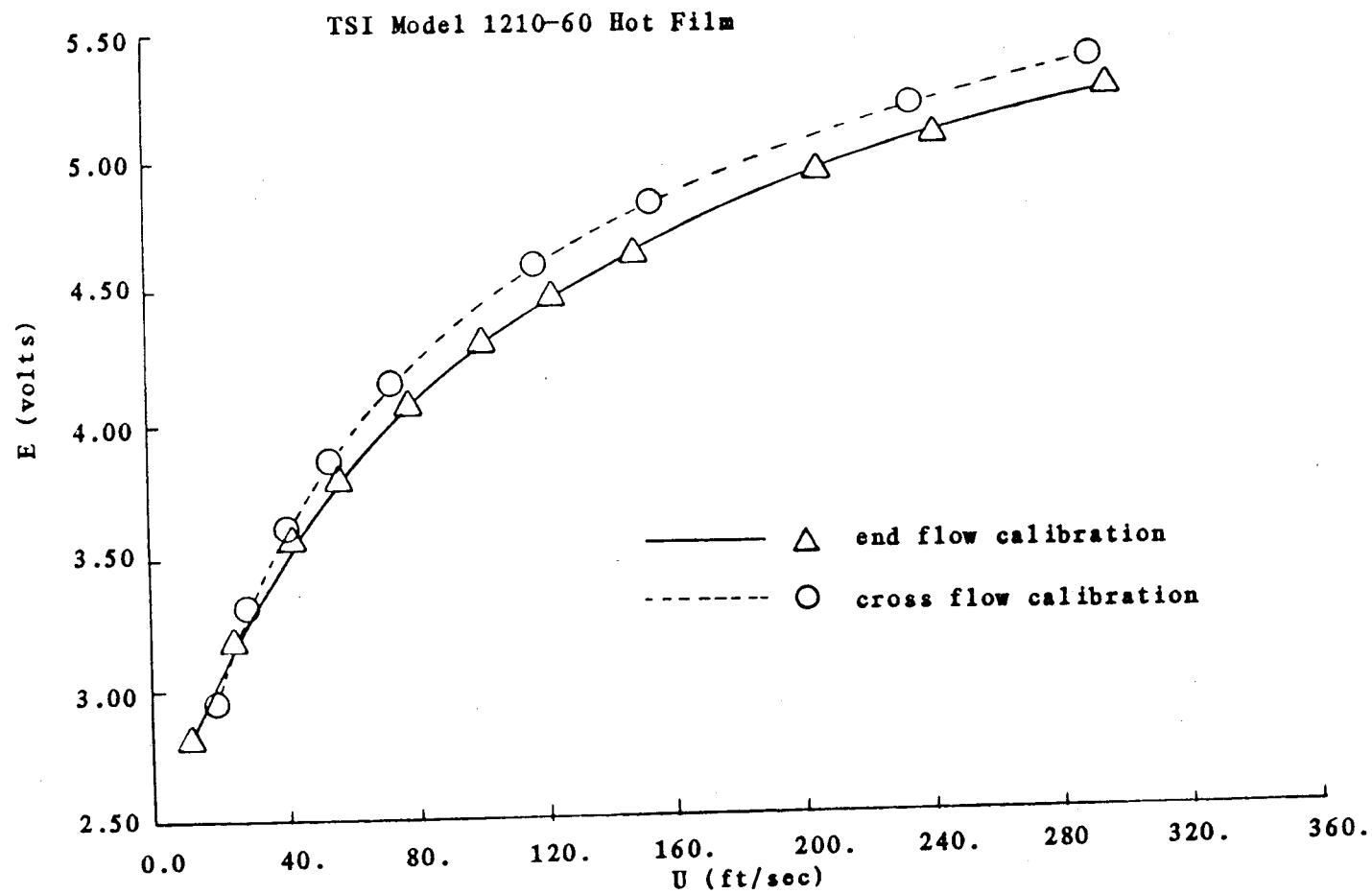
Figure 36. Cross flow calibration compared with end flow calibration in four inch calibrator

LIST OF REFERENCES

1.   Shaw, R. J., 'Progress Toward the Development of an Aircraft Icing Analysis Capability', NASA TM 83562, presented at the 22nd Aerospace Sciences Meeting, Reno,Nevada, Jan 9-12, 1984.

2.   Olsen, W., Shaw, R. J., and Newton, J., 'Ice Shapes and the Resulting Drag Increase for a NACA 0012 Airfoil', NASA TM 83556, presented at the 22nd Aerospace Sciences Meeting, Reno, Nevada, Jan 9-12, 1984.

3.   Bragg, M. B., and Coirier, W. J., 'Aerodynamic Measurements of an Airfoil with Simulated Glaze Ice', AIAA-86-0484, presented at the 24th Aerospace Sciences Meeting, Reno, Nevada, Jan 6-9, 1986.

4.   Ingelman-Sundberg, M., and Trunov, O. K., 'Wind Tunnel Investigation of the Hazardous Tail Stall Due to Icing', Report No. JR-2, a joint report from the Swedish-Soviet working group on Flight Safety, 1979.

5.   Ranaudo, R. J., Mikkelsen, K. L., and McKnight, R. C., 'Performance Degradation of a Typical Twin Engine Commuter Type Aircraft in Measured Natural Icing Conditions', NASA TM 83564, presented at the 22nd Aerospace Sciences Meeting, Reno, Nevada, Jan 9-12, 1984.

6.   Brumby, R. E., 'Wing Surface Roughness, Cause and Effect', DC Flight Approach, Jan 1979, pp. 2-7.

7.   Gray, V. H., 'Prediction of Aerodynamic Penalties Caused By Ice Formations on Various Airfoils', NASA TN D-2166, Feb 1964.

8.   Bragg, M. B., 'Rime Ice Accretion and Its Effect on Airfoil Performance', Ph.D. Dissertation, The Ohio State University, Columbus, Ohio, 1981   also NASA CR 165599, 1982.

9.   Miller, T. L., Korkan, K. D., and Shaw, R. J., 'Statistical Study of an Airfoil Glaze Ice Drag Coefficient Correlation', SAE Technical Paper Series, 830753, presented at the Business Aircraft Meeting and Exposition, Wichita, Kansas, April 12-15, 1983.

10. Flemming, R. J. and Lednicer, D. A., 'Correlation of Airfoil Icing Relationships with Two-Dimensional Model and Full Scale Rotorcraft Icing Test Data', AIAA-85-0337, presented at the 23rd Aerospace Sciences Meeting, Reno, Nevada, Jan 14-17, 1985.

11. Eppler, R. and Somers, D. M., 'A Computer Program for the Design and Analysis of Low-Speed Airfoils', NASA TM 80210, Aug 1980.

12. Bragg, M. B., 'Predicting Airfoil Performance with Rime and Glaze Ice Accretions', AIAA-84-0106, presented at the 22nd Aerospace Sciences Meeting, Reno, Nevada, Jan 9-12, 1984.

13. Scott, J. N., Hankey, W. L., Giessler, F. J., and Gielda, T. P., 'Navier-Stokes Solution of the Flowfield Over Ice Accretion Shapes', AIAA-87-0099, presented at the 25th Aerospace Sciences Meeting, Reno, Nevada, Jan 12-15, 1987.

14. Potapczuk, M. G., 'Navier-Stokes Computations for a NACA 0012 Airfoil with Leading Edge Ice', AIAA-87-0101, presented at the 25th Aerospace Sciences Meeting, Reno, Nevada, Jan 12-15, 1987.

15. Cebeci, T., 'Interactive Boundary-Layer Analysis of Iced Airfoils', Airfoil Performance-in-Icing Workshop, NASA Lewis Research Center, July 17-18, 1986.

16. Bragg, M. B., and Coirier, W. J., 'Detailed Measurements of the Flow Field in the Vicinity of an Airfoil With Glaze Ice', AIAA-85-0409, presented at the 23rd Aerospace Sciences Meeting, Reno, Nevada, Jan 14-17, 1985.

17. Bragg, M. B., and Spring, S. A., 'An Experimental Study of the Flow Field About an Airfoil with Glaze Ice', AIAA-87-0100, presented at the 25th Aerospace Sciences Meeting, Reno, Nevada, Jan 12-15, 1987.

18. Boerner, T. H., and Leutheusser, H. J., 'Calibration of Split Fibre Probe for use in Bubble Two-Phase Flow', DISA Information, No. 29, Jan 1984, p. 10-13.

19. Schlichting, H., Boundary Layer Theory, 6th ed., McGraw-Hill, New York, 1968, p. 758-776.

20. Rae, W. H., Jr. and Pope, A., Low-Speed Wind Tunnel Testing, 2nd ed., John Wiley and Sons, New York, 1984, p. 344-444.

21. Bragg, M. B., and Gregorek, G. M., 'Wind Tunnel Investigation of Airfoil Performance Degradation Due to Icing', AIAA-82-0582, presented at the 12th Aerodynamic Testing Conference, Williamsburg, Virginia, March 22-24, 1982.

22. Khodadoust, A., 'A Flow Visualization Study of the Leading Edge Separation Bubble on a NACA 0012 Airfoil with Simulated Glaze Ice', Master's Thesis, The Ohio State University, 1987.

23. Squire, H. B. and Young, A. D., 'The Calculation of the Profile Drag of Aerofoils', R.A.E. Reports and Memoranda No. 1838, Nov. 18, 1937, p. 196-222.

24. Lomas, C. G., Fundamentals of Hotwire Anemometry, Cambridge University Press, New York, 1986, p. 1-5.

25. King, L. V., 'On the Convection of Heat from Small Cylinders in a Stream of Fluid: Determination of the Convective Constants of Small Platinum Wires with Applications to Hot-Wire Anemometry', Proc. Roy. Soc. (London), Vol. 214A, No. 14, p. 373, 1914.

26. Kreith, F., Black, W. Z., Basic Heat Transfer, Harper and Row, New York, 1980, p. 249-253.

27. Wills, J. A. B., 'The Correction of Hot-Wire Readings for Proximity to a Solid Boundary', J. Fluid Mech., Vol. 12, Part 3, 1962, p. 388-396.

NASA
National Aeronautics and Space Administration

Report Documentation Page

1. Report No. NASA CR-180847	2. Government Accession No.	3. Recipient's Catalog No.

4. Title and Subtitle	5. Report Date
An Experimental Mapping of the Flow Field Behind a Glaze Ice Shape on a NACA 0012 Airfoil	January 1988
	6. Performing Organization Code

7. Author(s)	8. Performing Organization Report No.
Samuel A. Spring	None
	10. Work Unit No. 505-68-11

9. Performing Organization Name and Address	11. Contract or Grant No.
The Ohio State University Dept. of Aeronautical and Astronautical Engineering Columbus, Ohio 43210	NAG3-28
	13. Type of Report and Period Covered

12. Sponsoring Agency Name and Address	Contractor Report Final
National Aeronautics and Space Administration Lewis Research Center Cleveland, Ohio 44135-3191	14. Sponsoring Agency Code

15. Supplementary Notes

16. Abstract

The flow field about a NACA 0012 airfoil with a simulated glaze ice shape was studied. Split hot-film anemometry was used to measure the streamwise velocity component in the upper and lower separation bubbles aft of the glaze ice horns. Velocity profiles were presented as well as the boundary layer momentum and displacement thickness distributions through the bubbles. Data were presented at angles of attack of zero, two and four degrees and clearly showed the large region of reverse flow. A detailed discussion of split hot-film acquisition and data reduction, and possible sources of error has been included.

17. Key Words (Suggested by Author(s))	18. Distribution Statement
Aircraft icing Iced airfoil flowfield measurements Computer code validation date	Unclassified – Unlimited Subject Category 02

19. Security Classif. (of this report)	20. Security Classif. (of this page)	21. No of pages	22. Price*
Unclassified	Unclassified	83	A05